ABSTRACT

SINGLA, VINOD KUMAR. A Theoretical Framework for Property Enhancement of Smart Materials Based on Manufacturing Process Modeling Using Artificial Neural Networks. (Under the direction of Dr. Fuh-Gwo Yuan).

Recent advancements in technologies such as structural health monitoring have accelerated the demand for sensors and actuators. Researchers across the world have been engaged in search of new materials and manufacturing techniques that can be utilized to produce devices which are affordable and perform better than their predecessors. Materials discovery is traditionally known to take between two to three decades to bring a product to market. On the other hand, improvements in manufacturing technology can be achieved much sooner. One of the ways to meet the stringent demands for quality and achieve enhancement of properties for short term gains, is by selecting the manufacturing process parameters in the best possible way. Selection of these process parameters in an optimal manner, so that a property enhancement can be achieved, requires development of a computational model that can accurately emulate the manufacturing process. Due to the sheer number of process parameters and complexity of phase transitions involved in manufacturing of smart materials, it is difficult to develop a conventional model for process optimization and property enhancement. In the last decade, artificial neural networks have become increasingly popular for their ability to capture highly non – linear physical phenomena. In this work, a theoretical framework for modeling manufacturing processes of smart materials is developed using artificial neural networks. To this end, a novel artificial neural network architecture which can emulate the manufacturing process accurately is proposed. Thereafter, the mathematics involved in training additional weights in the proposed cascaded artificial neural network (CANN) is developed. Using data generated artificially and implementations in Python, a comparison between performance of traditional and cascaded artificial neural networks has been made. Finally, by coupling the artificial neural network model of manufacturing process with an evolutionary optimization paradigm such as genetic algorithm and tweaking the manufacturing process parameters, the prospect of property enhancement in smart materials is explored.

A Theoretical Framework for Property Enhancement of Smart Materials Based on Manufacturing Process Modeling Using Artificial Neural Networks

by
Vinod Kumar Singla

A thesis submitted to the Graduate Faculty of
North Carolina State University
in partial fulfillment of the
requirements for the degree of
Master of Science

Mechanical Engineering

Raleigh, North Carolina

2018

APPROVED BY:

_____	_____
Dr. Paul Ro	Dr. Yun Jing

_____
Dr. Fuh-Gwo Yuan
Chair of Advisory Committee

DEDICATION

To my family for always believing in me.

BIOGRAPHY

The author was born on September 8, 1991 in a small town filled with lush green fields named Bhadaur, India. He attended the Indian School of Mines, Dhanbad for his bachelor's degree in Mechanical Engineering. After completing his undergraduate studies in 2014, he joined FMC Technologies Pvt. Ltd. as an application engineer where he worked for the next two years. Aiming to expand his technical horizons, the author decided to pursue a master's degree at North Carolina State University, Raleigh in 2016. During his stay at NC State, the author has been a member of Smart Structures and Materials Laboratory (SSML) led by Dr. Fuh-Gwo Yuan and exploring techniques for property enhancement of smart materials.

ACKNOWLEDGMENTS

I would like to thank Dr. Fuh-Gwo Yuan for giving me the opportunity to work under his guidance. Dr. Yuan has been a great mentor and provided persistent direction and support throughout my stay at NC State. I would like to thank the committee members, Dr. Paul Ro and Dr. Yun Jing for taking the time out of their busy schedules to serve on my thesis committee and for the courses they have taught me.

I would like to thank the Department of Mechanical and Aerospace Engineering at NC State for giving me the opportunity to pursue graduate studies and support in the form of a teaching assistantship. Being a part of the student community at NC State is an amazing experience and the hands-on curriculum adequately prepares the student for taking on any challenges in life.

I would like to especially thank my parents for their love, patience and sacrifices in affording me a quality education. I admire them for their strength and courage in giving me the freedom to pursue my dreams thousands of miles away from home. I would like to thank my sisters Shweta and Rachna for their help and constant encouragement.

I would also like to thank my lab mates, in particular, Sakib, Karthik and Chao for making this journey memorable and providing motivation when it was most needed. A special thanks to my flat mates Ankur, Chinmoy, Rachit and Moharnab for their help in making the transition into a new life both easier and enjoyable. Finally, I would like to thank God for making me the person I am today.

TABLE OF CONTENTS

LIST OF TABLES

LIST OF FIGURES

1. INTRODUCTION

1.1 Background

Smart materials have been ubiquitous in commercial applications ranging from aerospace [1], seismic isolation [2], civil [3], and biomedical [4]. Due to the multibillion dollar potential for business opportunities in case of smart materials, their development is of considerable interest. A major impediment in bringing a new material to market is the sheer amount of time involved in materials discovery. Often the times range from two to three decades in research and development of a new material for some applications [5].

A growing field of interest in case of smart materials is that of property enhancement of existing smart materials. By varying the composition or addition of an impurity, researchers have been attempting to gain insights into the complex physical phenomena undergoing at the microscopic level in order to achieve property enhancement. The reason behind increased interest in property enhancement for smart materials is because in case of many applications, incremental improvements in figure of merits provide competitive edge in an ever-growing global materials market.

Traditional approaches to property enhancement and materials discovery have been mainly guided by intuition or trial and error. More recently, other approaches such as the use of first principle calculations to predict material properties [6], machine learning based materials design [7–9] and combinatorial experiments [10] have become popular for accelerating the pace of materials discovery and property enhancement. However, the idea of utilizing manufacturing process modeling for enhanced material properties is relatively new. Moreover, process modeling so far has largely been utilized for modeling only a part of the manufacturing process and not the whole process chain [11].

In this work, a framework of property enhancement by modeling the manufacturing process chain with artificial neural networks is presented. Towards this end, a novel artificial neural network architecture is proposed, and mathematics involved in the training the network is developed. By coupling the artificial neural network model of manufacturing process with an evolutionary optimization paradigm such as genetic algorithm and tweaking the manufacturing process

parameters, the prospect of property enhancement in smart materials is explored. Figure 1.1 provides a big picture view of the approach. A detailed discussion is presented in Chapter 4.

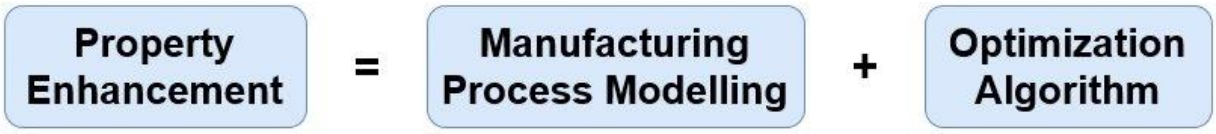

Figure 1.1 Big picture view of the proposed approach.

1.2 Thesis Outline

Since the property enhancement approach is developed in context of smart materials, a thorough survey has been performed on four classes (piezoelectric, electrostrictive, shape memory alloys and magnetostrictive) of smart materials. Chapter 2 provides insights into the phase transitions, physical phenomena and parameters that appear to the govern figures of merit in smart materials. This is followed by a discussion of the manufacturing techniques of most popular smart material in each of the four classes. For example, fabrication of lead zirconate titanate is discussed in case of piezoelectric materials and fabrication of Terfenol – D is discussed in case of magnetostrictive materials.

In chapter 4, a cascaded artificial neural network (CANN) architecture is proposed for process modeling along with the development of equations for the training process of additional weights (modified backpropagation). Thereafter, performances of both traditional and cascaded artificial neural networks are compared using Python implementations and data generated artificially. Coupling this artificial neural network architecture with a stochastic non – linear optimization algorithm is believed to yield a set of optimum process parameters for property enhancement. Finally, the work is concluded with a brief summary and future work.

2. SMART MATERIALS OVERVIEW

2.1 Piezoelectric Materials

The word “piezo” comes from Greek piezein which means to squeeze or press. This makes piezoelectricity synonymous with “pressure electricity”. More formally, materials that can generate charge/voltage on application of pressure are called piezoelectric materials. This phenomenon was first discovered in a Quartz crystal by Pierre and Jacques Curie in 1880. Conversely, piezoelectric materials can also deform in response to an applied electric field. When a deformation generates an electric field (sensors), the phenomenon is referred to as “direct piezoelectric effect”. On the other hand, if an applied electric field causes a geometric strain (actuators), we call it “converse piezoelectric effect”. Due to their ability to be utilized as both sensors and actuators, piezoelectric materials have been widely used in applications such as medical imaging, structural health monitoring, radar, sonar etc.

2.1.1 Origin of Piezoelectricity

Most piezoelectric materials are insulators and contain a large proportion of bound charges. A bound charge is a pair of equal and opposite point charges separated by a distance. Such a pair of point charges separated by some distance is called an electronic dipole. As the charges are bound, application of an electric field to an insulator material does not result in charge conduction. However, it produces a motion of point charges resulting in an overall polarization of the material. Figure 2.1 represents dipoles in an insulator material before and after the application of an electric field. As it can be seen, the dipoles have reoriented themselves to neutralize the effect of applied electric field and reach a low energy state.

This is accompanied with a geometric strain in the material which is directly proportional to the applied electric field. Conversely, a geometric strain in the material can induce polarization in the material and result in a net electric field. Piezoelectric materials are crystalline solids and do not possess an inversion center. A collection of individual crystals called unit cells forms the three-dimensional structure of these materials. Unit cells are classified into 32 crystallographic classes or point groups and piezoelectric materials belong to one of the 21 non-centrosymmetric crystallographic classes. Since, lack of a center of symmetry is a necessary condition for a material

to exhibit piezoelectric properties, all piezoelectric materials are intrinsically anisotropic. Piezoelectric materials are further classified into pyroelectrics and non-pyroelectrics based on the presence or absence of a mean dipole moment in the unit cell.

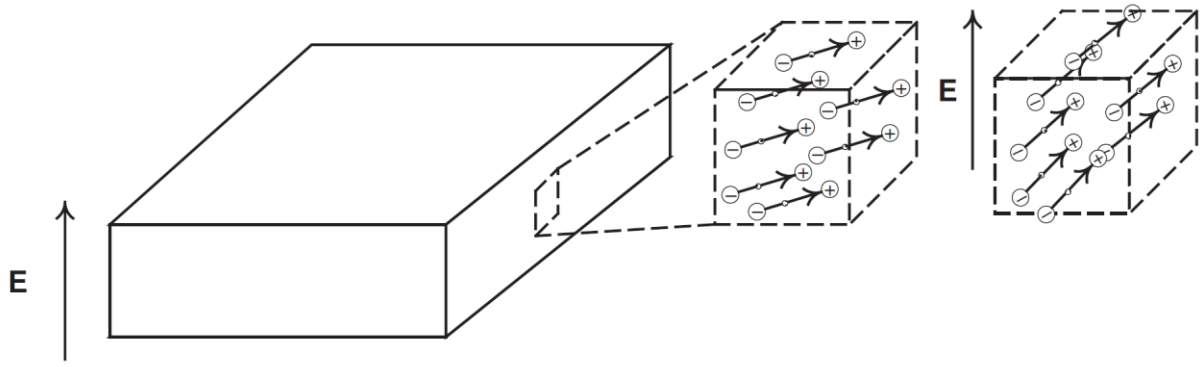

Figure 2.1 Dipoles in an insulator material before and after the application of electric field [12].

The mean dipole moment can be reversed by an external electric field for a subset of pyroelectrics called ferroelectrics. On heating above a certain temperature, ferroelectrics lose their piezoelectric and ferroelectric properties and become paraelectric. This temperature is commonly known as the "Curie point" and plays an important role in deciding the operating temperature range in most piezoelectric applications.

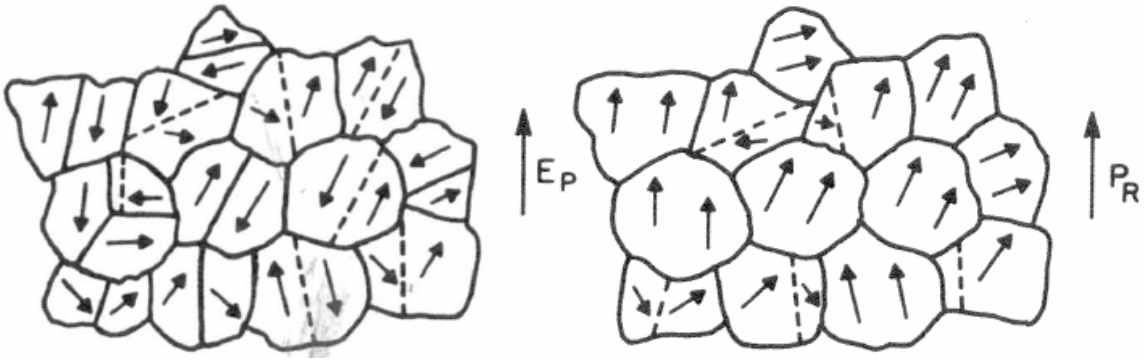

(a) (b)

Figure 2.2 Grain structure of a piezoelectric ceramic (a) Unpoled (b) Poled.

It is noteworthy to mention that a large class of piezoelectric materials are polycrystalline ferroelectric ceramics. Manufacturing of these materials results in a random grain structure and centrosymmetric material with no piezoelectric properties. A further "poling" process is required

to induce piezoelectric properties in these materials. Figure 2.2 shows the grain structure of a piezoelectric ceramic before and after the poling process. In the first case, the domains are randomly oriented, and the material has no overall polarization ($P_R = 0$). However, application of an electric field (E_P) just below the Curie temperature results in rotation of domain walls and associated dipoles which results in net polarization ($P_R \neq 0$) along the poling axis. This leads to high piezoelectric properties along the poling axis.

2.1.2 Figures of Merit for Piezoelectric Materials

In case of piezoelectric materials, the most important figures of merit are: piezoelectric strain coefficient d , piezoelectric voltage coefficient g , the electromechanical coupling coefficient k , the mechanical quality factor Q_m , and the acoustic impedance Z [13].

The piezoelectric strain coefficient relates the strain induced ε in the material to an applied external electric field E , i.e.

$$\varepsilon = dE \tag{2.1}$$

The piezoelectric voltage coefficient relates the induced electric field E in the material to applied external stress T , i.e.

$$E = gT \tag{2.2}$$

The electromechanical coupling coefficient for a piezoelectric material is a measure of the effectiveness of electromechanical energy conversion. It provides the fraction of input mechanical energy converted to stored electrical energy when an external stress is applied on the piezoelectric material. Conversely, it also provides the fraction of input electrical energy converted to stored mechanical energy when an external electric field is applied on the piezoelectric material.

$$k^2 = \text{(Stored electrical energy/Input mechanical energy)} \tag{2.3}$$

or

$$k^2 = \text{(Stored mechanical energy/Input electrical energy)} \tag{2.4}$$

The mechanical quality factor, Q_m is given by an inverse of mechanical loss and determines the frequency characteristics of the piezoelectric material.

$$Q_m = 1/\tan\delta \tag{2.5}$$

For ultrasonic applications, a high Q_m is usually preferred to minimize heat generation by mechanical loss. However, for sensor applications, a low Q_m is desired to cover a wide frequency spectrum.

The acoustic impedance, Z is a measure of acoustic energy transfer between two materials. In case of solid materials, it is given by;

$$Z = \rho c \tag{2.6}$$

where ρ is the density and c is the speed of sound in the material.

2.1.3 Barium Titanate, Lead Zirconate Titanate and Polyvinylidene Fluoride

Compact radar systems development during World War II accelerated the search for high permittivity dielectric materials for multilayered capacitors. Independent doping studies of TiO_2 with BaO by researchers in United States, Japan and Russia led to the discovery of barium titanate (BT) which had an enhanced dielectric permittivity. In addition, superior piezoelectric properties of BT conflicted with the belief at the time that polycrystalline materials cannot exhibit direct or converse piezoelectric effect. It wasn't clear until a few years later that the superior piezoelectric properties of BT were due to the poling process. This was first clearly recognized by R. B. Gray of Erie Resistor Company [14] and independently by Shepherd Roberts at MIT [15]. The perovskite crystal structure of BT above its Curie point is shown in Figure 2.3.

Although BT had a reasonably high piezoelectric coupling coefficient, a low Curie temperature of 120 ◌̊C leads to an aging effect during which the coupling coefficient can decrease by up to 15% over a year. Mason demonstrated that this was due to the loss of permanent polarization from the polarized ceramic [16]. In order to reduce the effects of aging on piezoelectric properties and increase Curie temperature, various ion replacements such as Pb^{2+} and Ca^{2+} in place of Ba^{2+} were

studied. As a result of these studies, a new ceramic piezoelectric material, Lead Zirconate Titanate (PZT) was discovered.

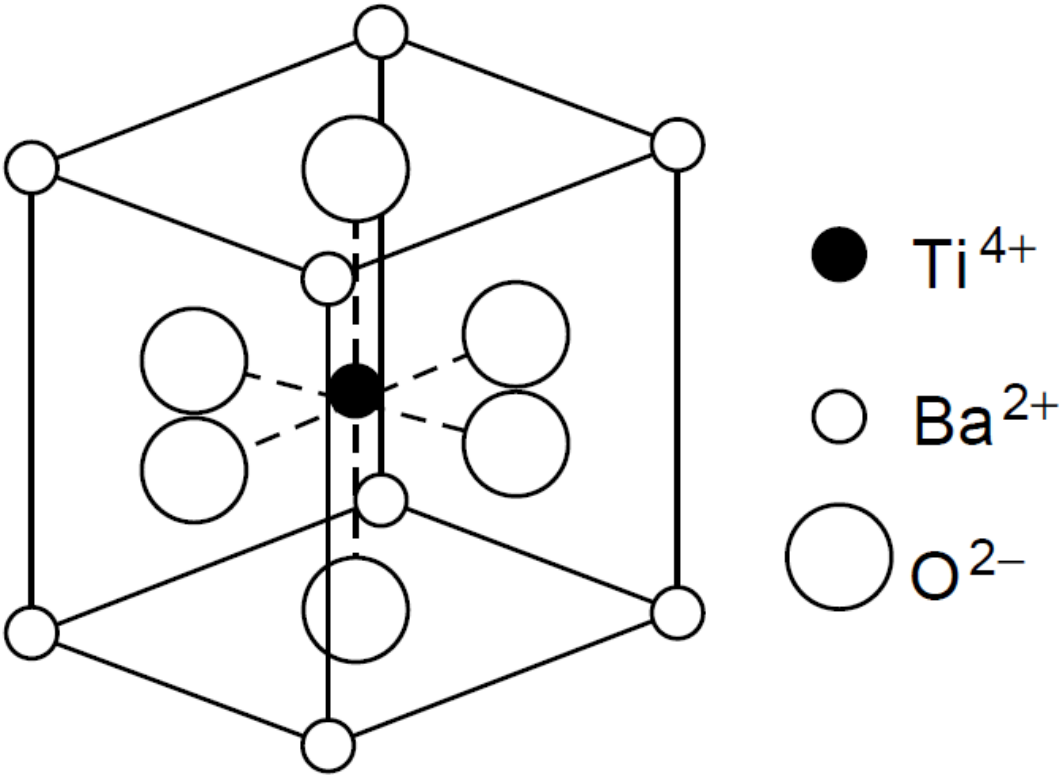

Figure 2.3 Crystal structure of $BaTiO_3$ [17].

PZT is a binary solid solution of lead zirconate ($PbZrO_3$) and lead titanate ($PbTiO_3$) and has a perovskite crystal structure similar to BT. At a particular mole percent of lead titanate in the solid solution, the piezoelectric properties of PZT are considerably enhanced. Moreover, this composition remains relatively constant with temperature. Below this composition, the material exists in a rhombohedral phase and as we keep increasing the mole percent of lead titanate in the solid solution, there is a phase change to tetragonal phase. In case of PZT, the phase boundary occurs when Zr:Ti ratio is 52:48. The boundary separating the two phases is called "Morphotropic Phase Boundary" (MPB) and the mole percent at which this happens is referred to as morphotropic composition. The temperature independence of morphotropic composition in case of PZT is usually characterized by referring the phase boundary as a "vertical" MPB. Phase diagram for the $Pb(Zr, Ti)O_3$ solid solution is given in Figure 2.4.

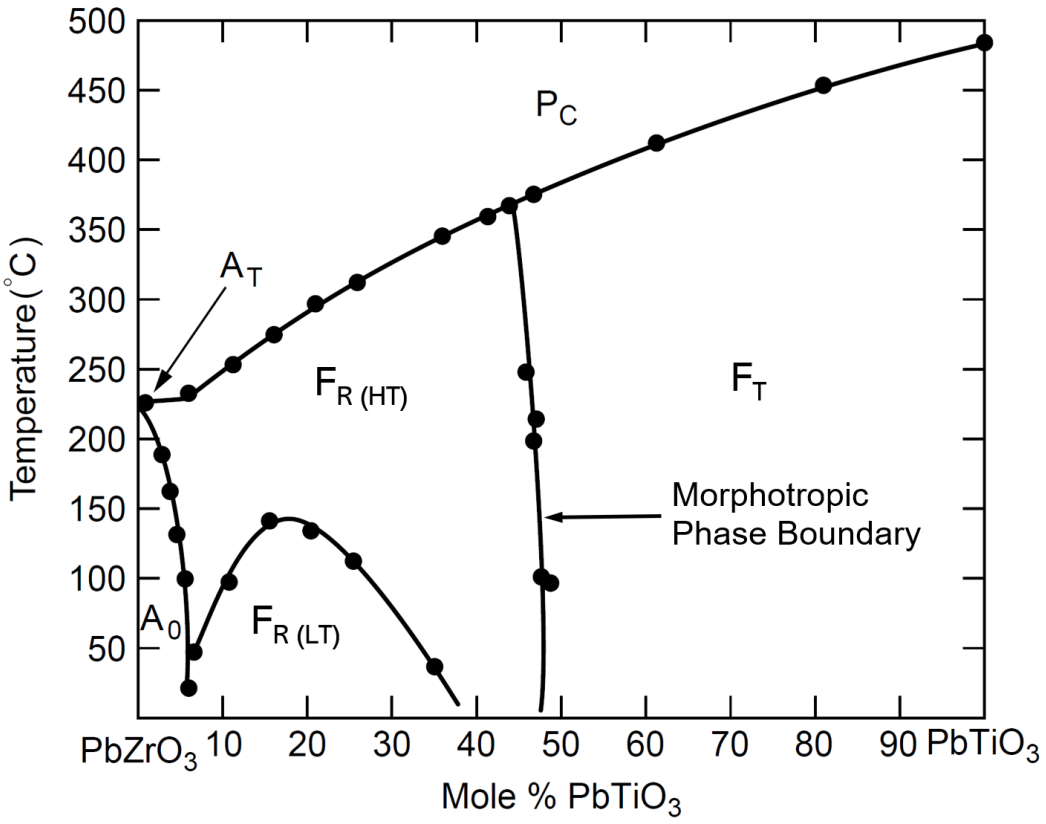

Figure 2.4 Phase diagram for Pb(Zr, Ti)O_3 solid solution [13].

The legend for different phases in Figure 2.4 is given below:

A_T = antiferroelectric tetragonal

A_0 = antiferroelectric orthorhombic

$F_{R(HT)}$ = ferroelectric rhombohedral (high temperature form)

$F_{R(LT)}$ = ferroelectric rhombohedral (low temperature form)

F_T = ferroelectric tetragonal

P_C = paraelectric cubic

PZT is a commercially important material due to a broad range of its applications. This is because the composition of PZT can be modified to serve the needs of a particular application. For example, applications wherein large piezoelectric properties are required, MPB composition is selected.

However, if stability of piezoelectric properties with respect to change in temperature or pressure is desired, a composition away from MPB and rich in tetragonal phase is selected. This is because tetragonal PZT has good temperature stability and a high Curie temperature which makes it suitable for such an application.

PZT can also be doped with impurities to change its piezoelectric properties dramatically. Takahashi [18] proposed that this is due to changes in ferroelectric domain configurations within the ceramics. If PZT is doped with acceptor ions such as K^+ or Na^+, it becomes more resistant to poling and depoling. This is usually accompanied with a reduction in other piezoelectric properties. However, if PZT is doped with acceptor ions such La^+, it becomes easier to pole and depole the material and other piezoelectric properties of PZT are increased. Depending on whether the doping is performed with acceptor or donor ions, doped PZT is referred to as "hard" or "soft". In general, hard PZT is used for resonant sensor/actuator applications where high Q_m and stable piezoelectric properties are required. On the other hand, soft PZT is usually employed for non-resonant sensor/actuator applications due to its large piezoelectric coefficient.

For applications where mechanical properties of a plastic material are required in combination with piezoelectric electromechanical coupling, conventional piezoelectric ceramics or single crystals cannot be utilized. In such cases, a flexible piezoelectric polymer material such as polyvinylidene fluoride (PVDF) is used. The piezoelectric phenomenon in PVDF was first reported by Kawai [19] in 1969. Poled thin films of PVDF were shown to exhibit piezoelectric coefficients in the range of 6 – 7 pC/N, which is roughly ten times larger than that observed in any other polymer. Interestingly, PVDF has a negative d_{33} value unlike most other piezoelectric materials which means that it will compress instead of expanding when subjected to the same electric field. Many of the properties of interest in case of PVDF are linked to the strong electrical dipole moment of the PVDF monomer unit ($5-8\times10^{-30}$ Cm) [20].

PVDF is a semi-crystalline polymer which can be present in 4 different crystal phases structures: the orthorhombic α, β, and δ phases and the monoclinic $\gamma-$phase; depending upon the processing and thermomechanical treatments performed on the material. The nonpolar $\alpha-$phase PVDF is formed by direct crystallization from the melt and has a trans-gauche conformation

(TG^+TG^-). The $\beta-$phase can be obtained by uniaxial or biaxial drawing of the $\alpha-$phase and reorienting the resulting dipoles through electrical poling. It is polar and has an all trans planar zig-zag conformation (TTT). The $\gamma-$phase PVDF is weakly piezoelectric and has a conformation consisting of a sequence of three trans linked to gauche ($TTTG^-$-$TTTG^+$). It is usually obtained by melt crystallization at extremely high temperatures and very slow cooling rates. The $\delta-$phase, which is nothing but a polarized $\alpha-$phase, can be obtained by applying a large electric field to nonpolar $\alpha-$phase PVDF. Note that, from an application point of view, the most important phase of PVDF is the $\beta-$phase due to its enhanced piezoelectric and pyroelectric properties [21–23]. Different crystal phase structures of PVDF are shown in Figure 2.5.

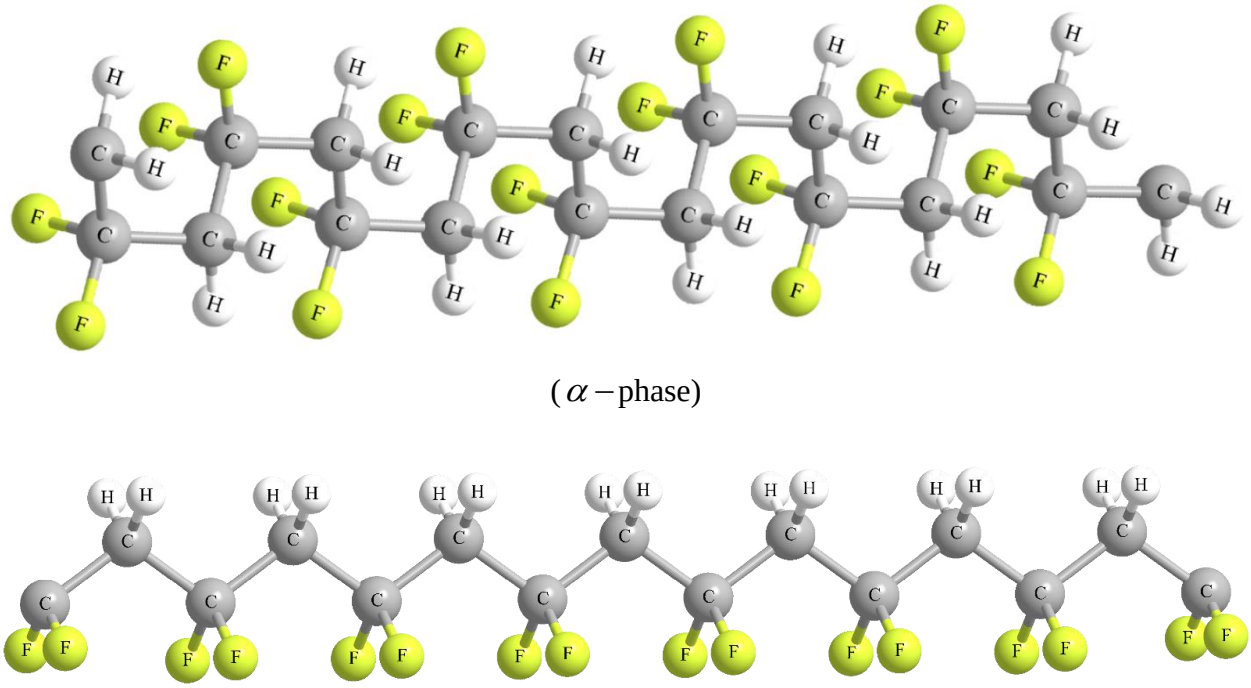

($\alpha-$phase)

($\beta-$phase)

Figure 2.5 Phase structures of PVDF.

2.1.4 Single Crystal Piezoelectric Materials

Conventional single crystal piezoelectric materials include quartz (SiO_2), lithium niobate ($LiNbO_3$), and lithium tantalate ($LiTaO_3$). Although piezoelectric coefficient of these materials is smaller than polycrystalline PZT, they are still extensively used in applications such as frequency-

stabilized oscillators and surface acoustic wave (SAW) devices. Note that these single crystals are anisotropic and possess different material properties depending upon the cut and direction of wave propagation.

Quartz has extremely high mechanical quality factor, $Q_m > 10^5$ which makes it a good candidate for resonance applications. Also, quartz has cuts with zero temperature coefficient i.e. properties of some quartz cuts do not change with temperature. For example, quartz oscillators are commonly used as clock sources in computers, TVs and VCRs. On the other hand, lithium niobate and lithium tantalate have very high electromechanical coupling coefficients for surface acoustic waves and are often used in SAW devices. In addition, Curie temperatures of lithium niobate and lithium tantalate are 1210 °C and 660 °C respectively and large single crystals for these materials can be easily obtained from their melt using the Czochralski technique [24].

More recently, single crystals of $Pb(Zn_{1/3}Nb_{2/3})O_3$ - $PbTiO_3$ (PZN-PT) and $Pb(Mg_{1/3}Nb_{2/3})O_3$ - $PbTiO_3$ (PMN-PT) have been shown to possess exceptionally large piezoelectric and electromechanical coupling coefficients. These materials have complex disordered perovskite structures and are a part of relaxor ferroelectrics family. Relaxor ferroelectrics deviate from normal ferroelectrics in three distinct ways. They have diffused phase transition from paraelectric to ferroelectric state, frequency dependent dielectric constant a.k.a. dielectric relaxation and weak remnant polarization [25, 26].

2.1.5 Lead-Free Piezoelectric Materials

Although several lead free piezoelectric materials such as barium titanate (BT), bismuth sodium titanate (BNT), bismuth potassium titanate (BKT), potassium sodium niobate (KNN), Bismuth layered structures (BLSF) etc. were originally discovered around the same time as PZT, their widespread adoption was limited due to poor piezoelectric properties in contrast with PZT [27]. Increased awareness and concerns regarding environment pollution caused by lead containing devices at the end of their life have led to several regulations [28–30] restricting its use. PZT, one of most important commercial piezoelectric materials contains 60% lead by weight. Its overall toxicity is further enhanced due to release of lead oxide vapor during synthesis. In light of this, there has been a concerted effort by the scientific community for the past three decades to develop lead-free piezoelectric materials whose properties are equivalent or better than PZT.

One of the first steps in this direction was a study of dielectric and piezoelectric properties of barium-modified bismuth sodium titanate, $\left(Bi_{1/2}Na_{1/2}\right)_{1-x}Ba_xTiO_3$ (BNT-BT) [31]. It was observed that a morphotropic phase boundary with enhanced electromechanical coupling factor and low free permittivity exists at x = 0.06~0.07. It should be noted that widespread investigation into lead-free ceramics was largely absent until the excitement and interest in this area was revived by the discovery of sodium potassium niobate, $(K,Na)NbO_3$ (KNN) based textured ceramic with PZT-like piezoelectric coefficients [32]. This was significant because for the first time, a lead free piezoelectrical material was shown to exhibit piezoelectric properties similar to that of PZT. More recently, superior piezoelectric strain coefficients have been reported for both KNN-based ($d_{33} = 570$ pC/N) [33] and BNT-based ($d_{33} = 1400$ pC/N) [34] ceramics.

Table 2.1 Material properties of representative piezoelectric materials.

Material	d_{33} (pC/N)	g_{33} $(10^{-3}Vm/N)$	k_p	k_p	$T_c(°C)$	$\tan\delta$	Q_m	**Ref.**
Quartz	2.3	57.8			-		$>10^5$	[13]
$BaTiO_3$	190	12.6	0.33		120			
PZT - 4	289	26.1	0.58		328		500	
PZT - 5H	593	19.7	0.65		193		65	
PVDF - TrFE	33	380			355		3-10	
BNTBT - 6	125				288	1.3		[31]
$(K_{0.44}Na_{0.52}Li_{0.04})(Nb_{0.84}Ta_{0.10}Sb_{0.06})O_3$	416	29.9	0.61		253			[32]
.91PZN - .09PT	2400			0.55		0.9		[35]
0.7PMN - 0.3PT	2280	34.2		0.62	140-150	<0.01		[36]

In general, lead free piezoelectric materials can be divided into three categories: perovskites, bismuth layer structured ferroelectrics and tungsten bronze type ferroelectrics. Lead free perovskites are believed to replace PZT in future due to their enhanced piezoelectric properties compared to other two categories. Material properties of representative piezoelectric materials for each of the categories discussed in previous sections are given in Table 2.1.

2.2 Electrostrictive Materials

Electrostriction is the basis of electromechanical coupling in all insulators (or dielectrics) [37]. In case of piezoelectric materials, the electromechanical coupling is modeled as a linear relationship between strain and applied electric field. However, in case of electrostrictive materials, the electromechanical coupling is represented as a quadratic relationship between strain and applied electric field. Figure 2.6 shows a representative relationship between induced strain and applied electric field in case of both piezoelectric and electrostrictive materials. Note that in reality, the induced strain is saturated on applying sufficiently large electric field in case of electrostrictive materials.

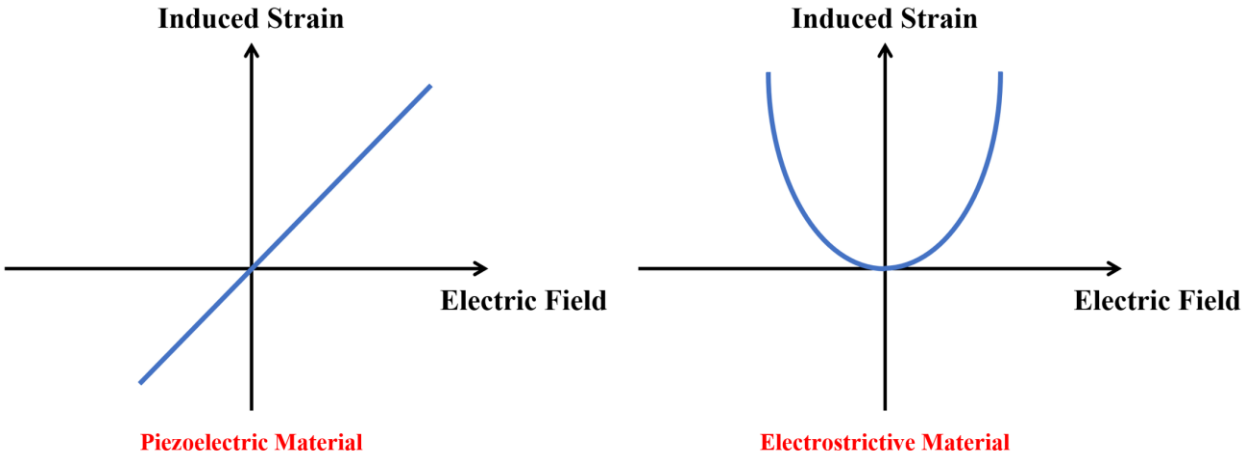

Figure 2.6 Relationship between induced strain and applied electric field for piezoelectric materials and electrostrictive materials.

In general, all dielectrics exhibit electrostriction to some degree whether they are crystalline, amorphous, polar or centrosymmetric. However, it is particularly large in a class of materials known as relaxor ferroelectrics. The first relaxor ferroelectric material was synthesized in 1961 [38]. However, electrostriction gained attention in the late seventies when relaxor ferroelectrics were utilized for precise positioning transducer application [39–43]. Since then, almost all of the commercial electrostrictive materials market has been captured by relaxor ferroelectrics. In comparison with PZT ceramics, the induced strain in relaxor ferroelectrics can be as high as 0.1% with minimum hysteresis (< 3%). Also, relaxor ferroelectrics do not require poling process to exhibit the electromechanical coupling. As a consequence, strain aging or creep is absent in these materials which makes them suitable for applications requiring a large number of load cycles unlike PZT ceramics.

There are two main modes of operation for electrostrictive materials namely the electrostrictive mode and the electric field biased piezoelectric mode. In the first mode, the material is operated just above its Curie temperature, T_c wherein the applied electric field stabilizes the ferroelectric phase leading to a large electrostrictive coefficient. This effect is more pronounced in relaxor ferroelectrics because T_c is spread out over a temperature range instead of being sharp resulting in a reasonable range of operation. However, in the field biased piezoelectric mode, a dc electric bias field is applied onto the material to induce ferroelectric polarization. Further, the material exhibits piezoelectric response proportional to applied electric field until saturation. The relationship between piezoelectric coefficient d_{33} (or d_{31}), electric polarization P, and dielectric permittivity ε_{33}, in field biased mode is given by equation (2.7) below [44].

$$d_{33} = 2Q_{11}P\varepsilon_{33} \text{ or } \left(d_{31} = 2Q_{12}P\varepsilon_{33}\right) \tag{2.7}$$

where Q_{11} and Q_{12} are longitudinal and transverse electrostrictive coefficients respectively. As briefly mentioned earlier, relaxor ferroelectrics deviate from normal ferroelectrics in three distinct ways. They have diffused phase transition from paraelectric to ferroelectric state, frequency dependent dielectric constant a.k.a. dielectric relaxation and weak remnant polarization. At high temperature, relaxor ferroelectrics exist in non-polar paraelectric (PE) phase and on cooling they transform into the ergodic relaxor (ER) state. In ER state, polar nanoregions (PNRs) with randomly distributed dipole moments emerge. The temperature at which PNRs appear is known as Burns temperature (T_B). Although there is no macroscopic or mesoscopic change in crystal structure accompanied with appearance of PNRs, the physical properties are changed dramatically. As the material is cooled further to a temperature $T_f < T_B$, the dynamics of PNRs is slowed and they freeze into a nonergodic state.

This is thought to be associated with the wide peak observed in variation of dielectric constant, ε with temperature. Unlike normal ferroelectrics, this peak is highly diffused and as the frequency of probing field is varied, the peak temperature $T_m (> T_f)$ shifts due to dielectric relaxation. The nonergodic relaxor (NR) state can be transformed into FE state by application of strong external

electric field. The material in FE phase can again be transformed to ER state by heating it to a temperature T_c [45].

Most commonly utilized electrostrictive materials include lead magnesium niobate (PMN), lead magnesium niobate – lead titanate (PMN - PT), lead lanthanum zirconate titanate (PLZT) and lead zinc niobate (PZN). Recent progress in each of these materials is reviewed in sections that follow.

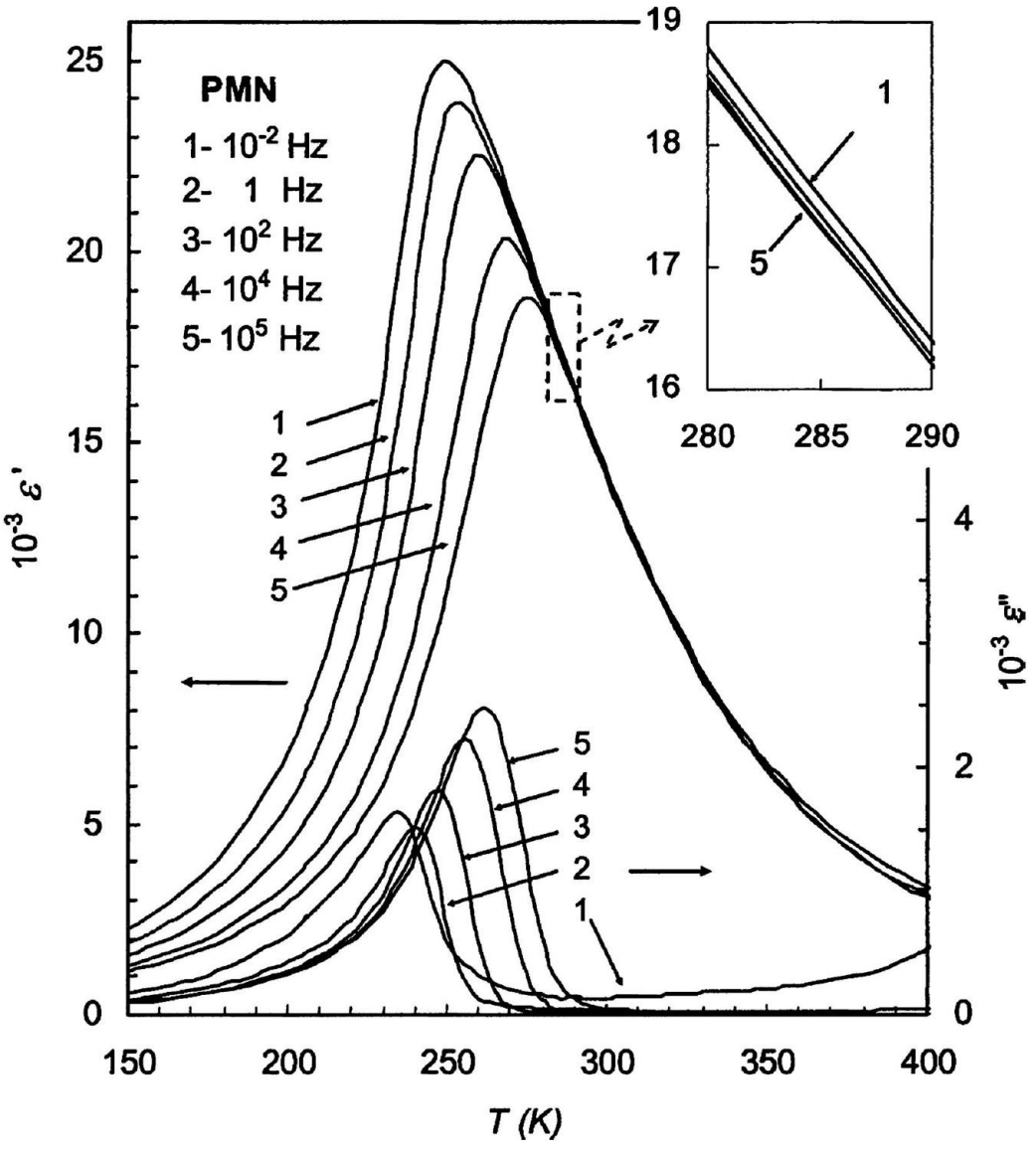

Figure 2.7 Temperature dependences of real and imaginary parts of the relative dielectric permittivity measured at different frequencies in a PMN crystal (Enlarged view in the insert shows the universal relaxor dispersion) [45].

2.2.1 Lead Magnesium Niobate (PMN)

PMN is a relaxor ferroelectric that possesses high permittivity ($\varepsilon \square 30,000$), diffused phase transition near room temperature and a large electrostrictive effect. The disorder that is responsible for the relaxor character of PMN is brought about by differences in valence (5^+ vs 2^+), ionic radii (0.64 vs 0.72 Å), and electronegativities (1.6 vs 1.2 on the Pauling scale) between the Nb^{5+} and Mg^{2+} ions, respectively, that introduce charge fluctuations and local disorder [46]. The variation of permittivity with temperature for PMN is shown in Figure 2.7. As it can be observed, the peak of permittivity shifts towards right as the frequency of probing field is increased. There have been several attempts to develop models for understanding this behavior [47, 48].

A recent physics model observed the presence of chemically ordered regions (CORs) of size less than 5 nm in addition to polar nanoregions in the PMN crystal. While CORs are stable and remain unchanged within a temperature range of $130-675$ K, PNRs show continuous growth with decrease in temperature. As the temperature is reduced below Curie temperature ($T < T_c$), adjoining PNRs coalesce to form micrometric domains in the ferroelectric state. These multiscale inhomogeneities in domain structure are thought to be a key driver in materials exhibiting relaxor behavior [49].

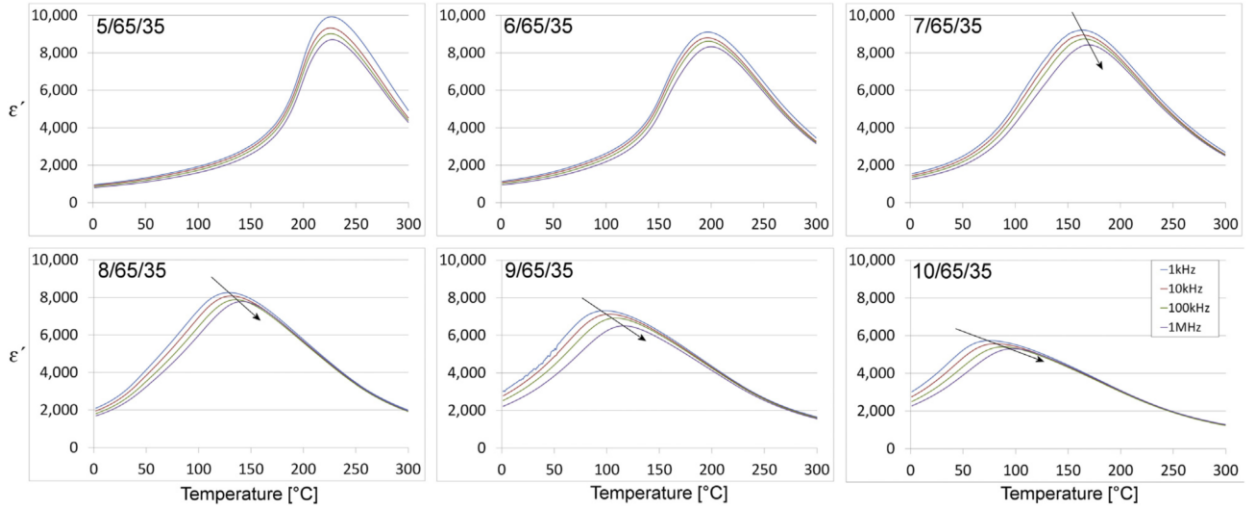

Figure 2.8 ε' vs T curves for y/65/35 PLZT compositions where 5 < y <10 [50].

Due its high dielectric and electrostrictive properties, PMN is a suitable material for several applications in electronics industry. However, difficulty in producing single – phase perovskite

material affordably has slowed its widespread adoption. The traditional fabrication technique of solid state reaction using mixed oxides results in formation of one or more stable lead-based pyrochlore phases which degrade the dielectric properties of the material. A number of other fabrication techniques: columbite method [51], wet chemistry routes [52–56], molten salt method [57, 58], mechanochemical method [59] etc. for the production of single perovskite phase PMN material have been explored. These will be discussed in detail in Chapter 3.

2.2.2 Lead Lanthanum Zirconate Titanate (PLZT)

Compositional modifications to PZT for achieving desired properties were briefly reviewed in the discussion of piezoelectric materials. As a reminder, doping PZT with acceptor ions results in increased resistance to poling and depoling (hard PZT) with a reduction in other properties. However, if PZT is doped with acceptor ions, it becomes easier to pole and depole the material (soft PZT) with an increase in other properties. Doping a solid solution of lead zirconate titanate (PZT) with lanthanum (La^{3+}, acceptor ion) results in enhanced relaxor characteristics and high optical transparency. This is believed to be a result of the vacancies caused by partial substitution of Pb^{2+} with La^{3+} ions on the A-sites of the ABO_3 perovskite crystal.

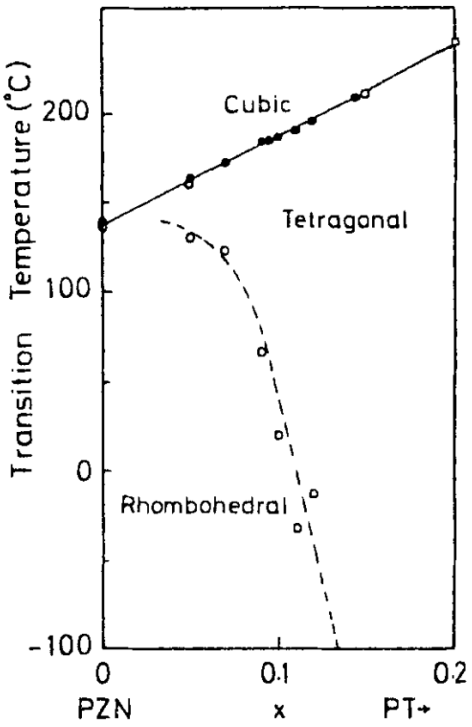

Figure 2.9 Phase diagram of PZN-PT solid solution [60].

The lanthanum modified lead zirconate titanate, PLZT ($Pb_{1-y}La_y(Zr_{1-x}Ti_x)_{1-y/4}O_3$) material with composition $x = 35$ and $y \in [5,10]$ has been extensively investigated because it exhibits relaxor behavior with a very high, broad and dispersive complex permittivity maximum [61]. Variation in real part of permittivity (ε') with lanthanum concentration is shown in Figure 2.8. It can be observed that increase in lanthanum concentration shifts the permittivity maximum to the left. Also, the dielectric dispersion becomes more pronounced for 7/65/35 PLZT composition and continues to increase towards 10/65/35 PLZT composition (see arrows).

In general, doping PZT with lanthanum results in increased squareness of the hysteresis loop, decreased coercive field (E_c), increased dielectric constant, increased mechanical compliance, maximum electromechanical coefficients and enhanced optical transparency. Note that for piezoelectric applications, lanthanum composition is usually less than or equal to 6 % whereas for electroptic applications it is more than 6%. In either case, the compositions are located around temperature independent morphotropic phase boundary which separates the ferroelectric rhombohedral and paraelectric tetragonal phases and maximizes properties of interest [61].

The fabrication of PLZT composition is usually done either by solid state reaction from mixed oxides or through chemical co-precipitation process. The subsequent consolidation or densification of PLZT is done by hot pressing or hot isostatic pressing. These techniques are discussed in Chapter 3.

2.2.3 Lead Zinc Niobate (PZN)

PZN is a relaxor ferroelectric with perovskite crystal structure. It exhibits diffused phase transition similar to PMN. PZN is a lucrative material for capacitors and actuators due to its high dielectric constant, excellent electrostrictive properties and high Curie temperature ($140°C$). However, the ceramic processing of PZN to prepare a powder composition is a challenge using conventional synthesis techniques. This is due to presence of a pyrochlore phase which results in poor properties. Several techniques to produce single perovskite phase PZN have been explored in the past including sol-gel processing, high pressure solid state reaction and solid solution with stable perovskites. Out of these, fabrication of PZN as a solid solution with other stable perovskites has proven to be more successful than others.

The solid solution of rhombohedral PZT with lead titanate, $PbTiO_3$ (PT) having a tetragonal crystal structure exhibits a morphotropic phase boundary (MPB) near 9 mole % PT. Single crystals of $PZN-PT$ with compositions near MPB (0.91 PZT – 0.09 PT) possess very high dielectric and piezoelectric coefficients in comparison with PZT. The phase diagram with different phases as the composition of PT is varied is shown in Figure 2.9. Typical values of coupling factor ($k = 0.92$) and piezoelectric coefficient ($d_{33} = 1500\,pC/N$) are highest among other materials at room temperature. Also, $PZN-PT$ is more stable than $PMN-PT$ and performs reliably at high temperatures due to its higher depolarization temperature [62]. A comparison between ferroelectrics and relaxor ferroelectrics is presented in the next section.

2.2.4 Comparison Between Normal Ferroelectrics and Relaxor Ferroelectrics

Differences between normal ferroelectrics and relaxor ferroelectrics were briefly highlighted in section 2.2.1. A detailed discussion is presented here and Figure 2.10 summarizes the comparison. As it can be seen from the polarization vs electric field ($P-E$) plot in Figure 2.10(a), there is large remnant polarization in case of normal ferroelectric. However, for relaxors the hysteresis is almost negligible. This is due to the presence of macro-sized ferroelectric domains in normal FEs which are permanently realigned on the application of electric field. On the other hand, the presence of polar nanoregions in relaxor materials implies that as soon as the applied electric field is removed, the random directions of PNRs are restored resulting in a very low remnant polarization.

As phase transition from rhombohedral to tetragonal phase usually takes place for a normal ferroelectric around Curie temperature T_c, the saturation and remnant polarization decrease when temperature is increased and vanish at the transition temperature (Figure 2.10(b)). Unlike normal FEs, relaxors retain finite values of saturation and remnant polarization well above the dynamic transition temperature Tm due to presence of PNRs. Also note that the phase transition near T_c for normal ferroelectrics can be first or second order and results in a macroscopic symmetry change. However, in a relaxor, there is no structural phase transition across T_m. The peak in dielectric constant value is usually attributed to slowed dipolar motion below T_m.

The dielectric constant ε' of normal FEs exhibits a sharp and narrow maximum at T_c. Interestingly, it is also frequency independent. In case of relaxors however, the peak is very broad and there is strong frequency dispersion in the peak temperature T_m as well as the magnitude of dielectric constant due to dipolar-glass like response of these materials (Figure 2.10(c)). Also, the normal ferroelectrics obey Curie-Weiss law i.e. $\varepsilon' = C/(T - T_0)$ above T_c for temperature dependence of dielectric constant. Relaxors on the other hand show strong deviation from this law. *C* is the Curie constant, *T* is current temperature and T_0 is the Curie point temperature in Curie – Weiss law mentioned earlier.

2.3 Shape Memory Alloys

Shape memory alloys (SMAs), in the past decades, have been actively employed for various industrial applications including but not limited to aerospace [1], seismic isolation [2], civil [3], and biomedical [4]. SMAs as a new functional material, have attracted engineers and researchers to utilize them in many engineering applications because they can reversibly recover their original shape with respect to temperature or stress variations. SMAs exhibit interesting nonlinear features in their stress-strain relationships; one of which is the shape memory effect, and the other is the pseudoelastic or superelastic effect [63–65].

Both represent a fundamental characteristic of large strain recovery of SMAs. It is known that SMAs can recover their original shape even after being deformed with 6 ~ 8% strain [66]. There is a clear departure of behavior from metals as the residual deformation can be recovered even if the applied loading is greater than the critical stress of the material. Furthermore, most SMAs are manufactured using metal-like materials and have sufficient strength expected of a practical engineering material. This allows SMAs to be employed for applications that involve heavy loading or stress. The prominent features of SMAs discussed above are caused by the phase transformations. Even though several types of SMAs have been investigated over the decades, perhaps, Nickel-Titanium (Ni-Ti) based SMA is one of the most popular material among metallic SMAs.

Ni-Ti SMAs can have two distinct phases with respect to temperature – one is martensite (M) and the other is austenite (A). These phases have properties that help distinguish one from the other.

To be specific, as martensite phase Ni-Ti SMA is heated, it starts to transition to the austenitic phase from a specific temperature and the phase of the material fully transforms to austenite on further heating. Later, when the SMA is cooled down, the austenitic phase begins to change to martensite and the SMA eventually becomes fully martensitic at a sufficiently low temperature [67]. The details involved in phase transformation will be discussed in the sections that follow. Emerging shape memory materials such as magnetic shape memory alloys (MSMAs) and shape memory polymers (SMPs) are also discussed.

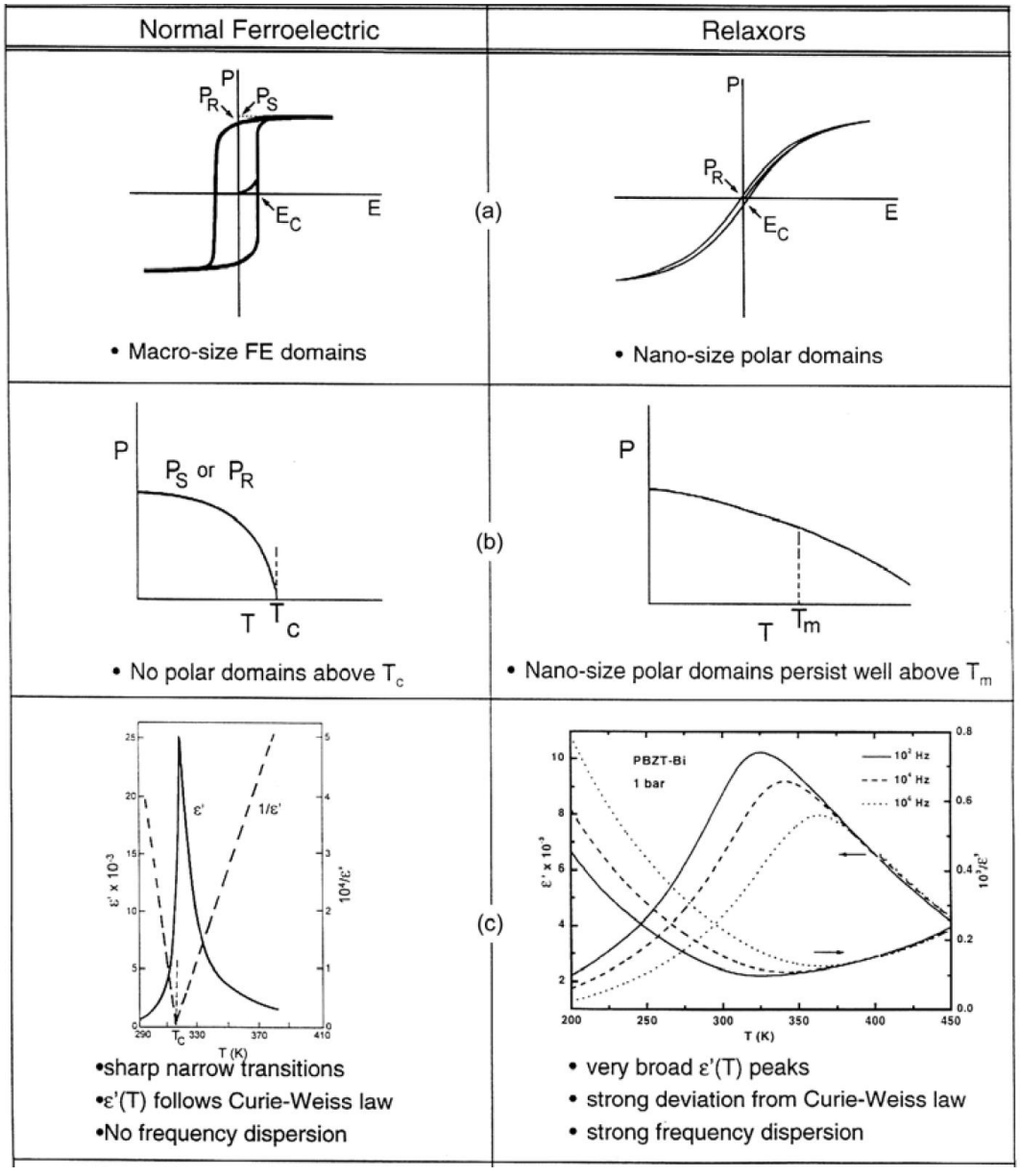

Figure 2.10 Comparison between properties of normal and relaxor ferroelectrics [68].

2.3.1 History and Recent Developments

The shape memory effect was initially observed by Arne Olander while working on completion of the phase diagram for gold (Au) – cadmium (Cd) [69] in the early 1930s. Later, Greninger and Mooradian observed the formation and disappearance of martensite phase in a copper (Cu) – zinc (Zn) alloy with variations in temperature [70]. The fundamental phenomenon of shape recovery in SMAs gained interest when it was reported by Kurdjumov and Khandros [71] in 1949 and independently by Chang and Read in 1951 [72]. However, significant advances in the research of SMAs had not been reported until the early 1960s.

Table 2.2 NiTi SMA material properties [73].

Property	**Units**	**Value**	
		Martensite	**Austenite**
Density	kg/m^3	6450 – 6500	
Electrical Resistivity (approx.)	μΩcm	76 – 80	82 – 100
Specific Heat Capacity	J/kg K	836.8	836.8
Thermal Conductivity	W/m K	8.6 – 10	18
Thermal Expansion Coefficient	$m/m\ K^{-1}$	6.6×10^{-6}	11.0×10^{-6}
Ultimate Tensile Strength	MPa	895	
Young's Modulus (approx.)	GPa	28 – 41	75 – 83
Yield Strength	MPa	70 – 140	195 – 690
Poisson's Ratio	–	0.33	
Magnetic Susceptibility	μemu g	2.5	3.8

Nitinol (Nickel-titanium Naval Ordnance Laboratory), perhaps the most common shape memory alloy, was discovered in 1959 by William J. Buehler at the Naval Ordinance Laboratory. Buehler was working on finding a suitable alloy of nickel (Ni) – titanium (Ti) for use in the nose cone of a

navy missile. He observed that the impact sound of the material varied with respect to temperature. Upon further investigation he concluded that the change in sound was due to change in structural elasticity of the material with temperature variations. This was the first discovery to demonstrate that a major structural alteration of a SMA can be brought about within a small temperature range [74–76]. We now have a much more deeper understanding of how changes in weight percent of individual elements and changes in temperature results in phase change in the Ti – Ni alloy system as demonstrated in the phase diagram given in Figure 2.11.

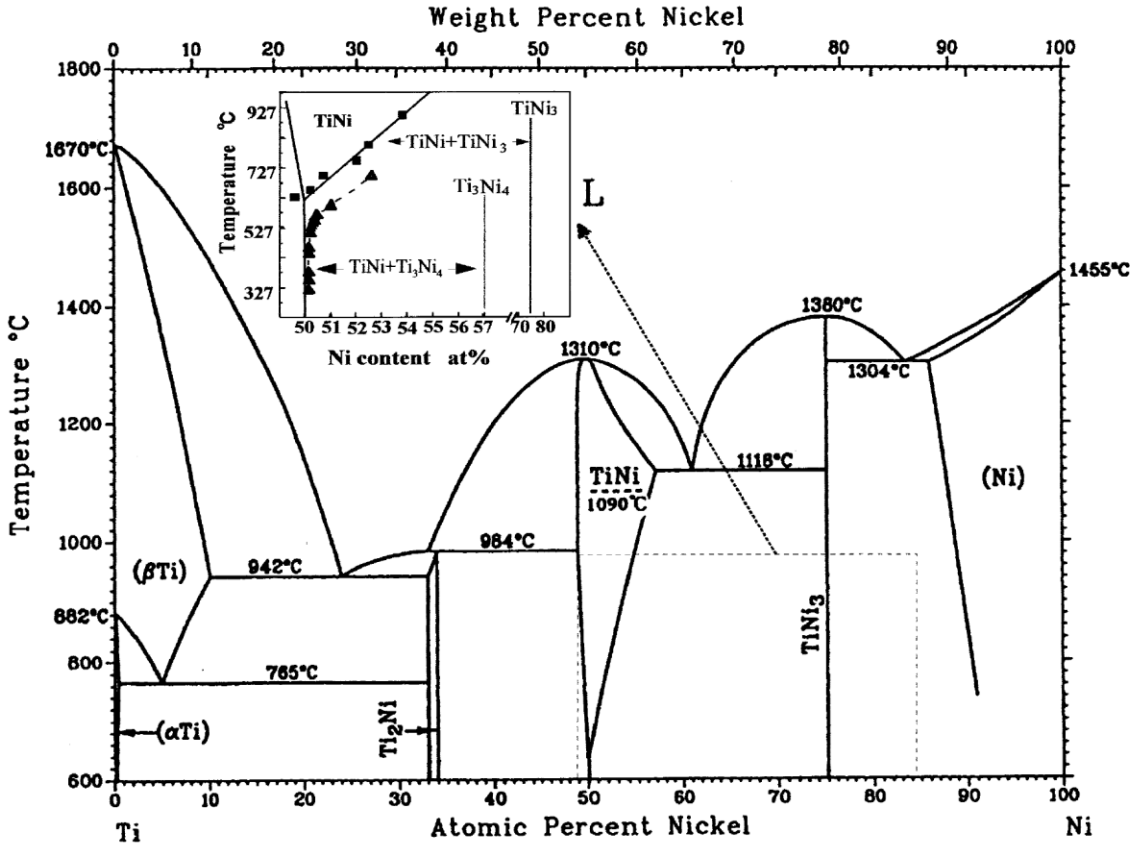

Figure 2.11 Phase diagram of Ti – Ni alloy [77].

Recently, nitinol alloys have become widely popular because they are cheaper to produce, safer to handle and have better mechanical properties than other SMAs (Au – Cd, Cu – Zn, Cu – Sn etc.). As mentioned earlier, they have been employed for a variety of industrial applications. Due to increase in demand, there has been a push to enhance SMA material properties. Researchers across the world are experimenting with different material compositions that result in improved material stability, wider operating temperature range, low stress & thermal hysteresis, recoverable &

irrecoverable strain, work output and easier fabrication techniques [8, 78–81]. Material properties of a commercial NiTi SMA are given in Table 2.2.

2.3.2 Shape Memory Effect and Pseudoelasticity

Depending upon variations in stress and temperature, nitinol SMAs can exist in three phases: austenite, twinned martensite (M^t), and detwinned martensite (M^d). Austenite has a body centered cubic (BCC) crystal structure and is stable at elevated temperatures. Both M^t and M^d on the other hand have a face centered cubic (FCC) crystal structure and are stable at low temperatures. The crystal structures of different phases of a nitinol SMAs are shown in Figure 2.12.

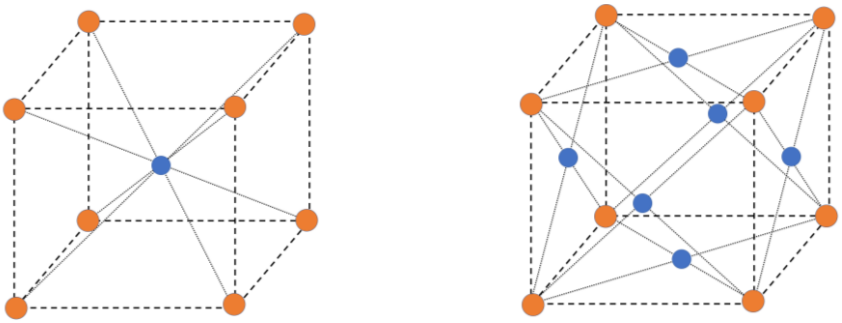

Figure 2.12 Crystal structure of nitinol SMAs (a) Austenite (b) Martensite.

There are four temperatures of interest for different phase transformations of nitinol SMAs. When a martensitic phase SMA is heated from a low temperature, it begins to transform into austenite. The temperature at which this begins to happen is called austenite start temperature (A_s). The temperature at which martensite phase has been completely transformed into austenite is called austenite finish temperature (A_f). Similarly, when austenitic phase SMA is cooled from high temperature, it begins to transform into martensite. The temperature at which this transformation starts is known as martensite start temperature (M_s) and the temperature at which it finishes is known as martensite finish temperature (M_f). Note that the above discussion is applicable for stress free material transformations. When is material is stressed, the transformation temperatures vary linearly as shown in Figure 2.13.

In addition to austenite to martensite transformation, the crystal structure of the material becomes less symmetric as the temperature is decreased and leads to formation of different variants of

martensite. For a low stress ($\sigma < \sigma_s$) and low temperature ($T < M_f$) condition, the neighboring domains present a twin or mirror-like structure relative to each other (self-accommodation). There is no change in length associated with this transformation and the martensite formed is known as twinned martensite. However, if the stress is sufficiently high ($\sigma > \sigma_f$) as the temperature is lowered, the material starts to deform while retaining atomic bonds and reaches a low energy state through detwinning. The detwinning process results in macroscopic shape change which is retained even when the load is released. The minimum stress required to start detwinning is called detwinning start stress (σ_s) and the stress required to complete detwinning of martensite is called detwinning finish stress (σ_f). Heating the detwinned martensite material to a temperature above results in phase transformation to austenite along with strain recovery.

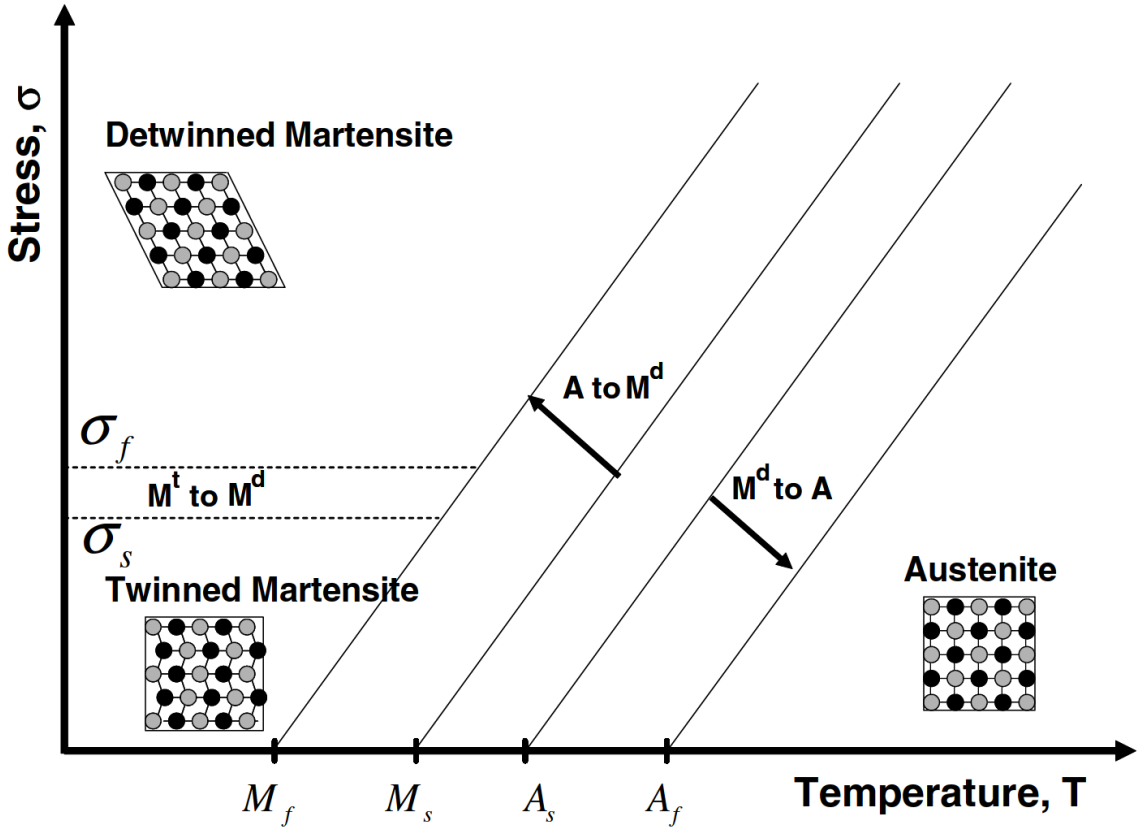

Figure 2.13 Schematic of stress-temperature phase diagram for nitinol SMA [82].

As discussed earlier, SMAs can recover their original shape even after severe plastic deformation. The origin of this phenomenon can be attributed to diffusionless solid phase transformation of high

temperature austenitic-phase into low temperature martensitic-phase and vice versa. When the strain recovery is performed at low temperature only by heating the material, the phenomenon is known as shape memory effect. On the other hand, if strain recovery is achieved at temperatures above A_f without any thermal activation i.e. by loading and subsequent unloading of the material, the phenomenon is called pseudoelastic effect.

Table 2.3 HTSMA material properties (PE: Pseudoelastic) [73].

Group ($^{\circ}C$)	**Composition**	**Transformation temperature range ($^{\circ}C$)**	**Thermal hysteresis ($^{\circ}C$)**	**Strain (%)**	**Recovery (%)**
100 – 400	Ni – Ti – Zr	100 – 250	54	1.8	100
	Ni – Ti – Hf	100 – 400	60	3	100
	Cu – Al – Ni		21.5	$3 - 5^{PE}$	$80 - 90^{PE}$
	Co – Al		121	2	90
	Ni – Mn – Ga		85	10	70
	Ti – Nb	100 – 200	50	$2 - 3$	$97 - 100$
	U – Nb		35	7	
400 – 700	Ti – Au	100 – 630	35	3	100
	Ti – Pd	100 – 510	40	10	88
	Ti – Ni – Pd	100 – 530	20 - 26	2.6 – 5.4	90^{PE} – 100
	Ti – Ni – Pt	110 – 1100	31 - 55	3 – 4	100
> 700	Ti – Pt – Ir	990 – 1184	66.5	10^{PE}	40^{PE}
	Ta – Ru	900 – 1150	20	4	50
	Nb – Ru	425 – 900		4.2	88

2.3.3 High Temperature Shape Memory Alloys

The phase transformation temperatures of NiTi SMAs limit its practical use to temperatures below 100 ℃. Because of this, application of NiTi based SMAs necessitates modification of components to reduce the operating temperatures. However, use of SMAs is even more lucrative at higher temperatures since an adaptive multifunctional component can reduce weight and lead to

significant savings over a complex multicomponent assembly. Exploration of such ideas by researchers have paved the way for a new class of SMAs with transformation temperatures above 100 °C. These materials are referred to as high temperature shape memory alloys (HTSMAs). They can be divided into three main categories based on their martensitic transformation temperatures. Group I has transformation temperatures in the range of 100 °C – 400 °C, Group II, in the range of 400 °C – 700 °C and Group III, above 700 °C. A summary of HTSMA material properties in each of the three groups is given in Table 2.3.

Increasing performance requirements for engineering applications necessitate SMAs to exhibit high recoverable strain, long term stability, resistance to hysteresis and high work output. As is evident in case of HTSMAs, these requirements become even more difficult to satisfy at elevated temperatures. This has prevented widespread commercialization of HTSMAs. Primary reason for this has been difficulty in processing due to low ductility and poor fatigue resistance at room temperature contributing to an increase in manufacturing costs. In spite of these challenges, better compositional control and alloying processes have led to several demonstrations of Ti-Ni-Pd and Ti-Ni-Pt being used for engineering applications [83].

2.3.4 Magnetic Shape Memory Alloys

Magnetic shape memory alloys (MSMAs) also known as ferromagnetic shape memory alloys (FSMAs) are a new category of multifunctional materials having magneto-mechanical coupling. Material strains of up to 10% can be induced and recovered in MSMAs which is significantly larger than recoverable strains in magnetostrictive materials like Terfenol-D. The reason behind magnetic field induced strains is thought to be microstructural reorientation of martensitic variants. These variants often have a preferred direction of magnetization which means magnetic field can be used to select one variant over the other resulting in macroscopic shape change.

MSMAs also exhibit conventional heat activated shape memory effect and stress activated pseudoelastic effect. However, the frequency of actuation for magnetic field induced strains is much higher, up to 1 kHz. This is because the reorientation of martensitic variants which drives their actuation happens much faster than heat transfer required for the shape memory effect. Despite having an advantage of faster actuation frequency, MSMAs have several other design issues.

The primary disadvantage of MSMAs is relatively low blocking stress levels (6 – 10 MPa) above which the magnetic field-induced strains disappear. In addition, MSMAs are very brittle, stiff and difficult to shape & form which has limited their utility in commercial applications. Most commonly investigated magnetic shape memory materials have been Ni – Mn – Ga alloys. Other magnetic shape memory alloys such as Fe – Pd, Fe – Pt, Co – Ni – Ga, Ni – Mn – Al and Co – N – Al have also been studied, however much work is still needed to develop a better understanding of their constitutive behavior to make them suitable for practical applications [82].

Table 2.4 Comparison of mechanical properties between SMAs and SMPs [84].

Property	Shape Memory Alloys	Shape Memory Polymers
Density, (g/cm^3)	6 – 8	0.9 – 1.1
Extent of deformation, (%)	< 8%	Up to 800%
Elastic modulus at $T < T_{tran}$, (GPa)	83	0.01 – 3.00
Elastic modulus at $T > T_{tran}$, (GPa)	28 – 41	$(0.1 – 10) \times 10^{-3}$
Stress required for deformation, (MPa)	50 – 200	1 – 3
Stress generated during recovery, (MPa)	150 – 300	1 – 3
Critical temperatures, ($^{\circ}C$)	-10 – 100	-10 – 100
Transition breadth, ($^{\circ}C$)	5 – 30	10 – 50
Recovery speeds	< 1 sec.	< 1 sec. – several min.
Thermal conductivity, (W/m-K)	18	0.15 – 0.30
Biocompatibility and biodegradability	Some biocompatible, not biodegradable	Can be both or any one
Processing conditions	> 1000 $^{\circ}C$, high pressure	< 200 $^{\circ}C$, low pressure
Corrosion performance	Excellent	Excellent
Cost, (per lb.)	~ $250	< $10

2.3.5 Shape Memory Polymers

NiTi SMAs have been commercially utilized for a number of applications over the years. However, despite their benefits, NiTi SMAs have limitations such as maximum recoverable strain (< 8%), high stiffness, high cost, limited transition temperature range and expensive processing conditions

that prohibit their use in certain applications. These limitations have motivated the research into low cost polymeric shape memory materials which can have much larger strains (> 200%).

Shape memory polymers (SMPs) are easy to manufacture and can be trained easily. In comparison with SMAs, they are biodegradable, cheaper (~ 10%), efficient (> 99%) and possess better mechanical properties. The three working mechanisms for shape memory effect in SMPs are: Dual-state mechanism, dual-component mechanism and partial-transition mechanism [85]. As in case of SMAs, the shape memory effect in SMPs depends on the material composition i.e. the weight fraction of switching segments and the molecular weight of the polymer-chain. It is worthwhile to note that despite their advantages, NiTi SMAs are preferred for applications requiring high actuation forces and fast response. A comparison of mechanical properties between SMAs and SMPs is given in Table 2.4.

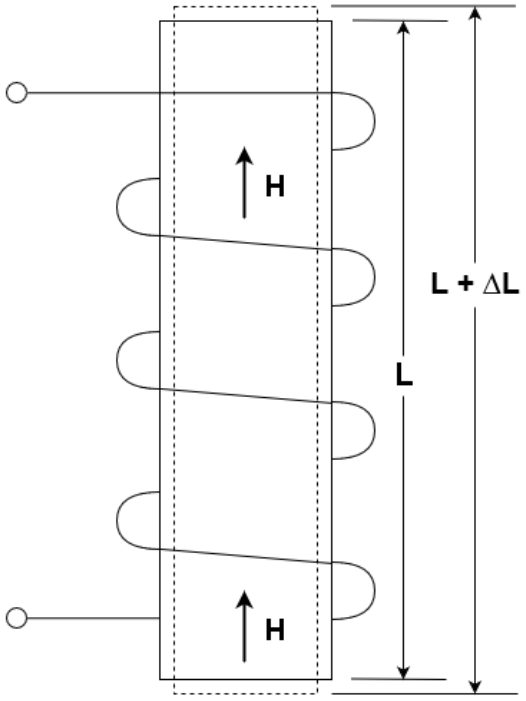

Figure 2.14 Example of Joule Magnetostriction.

2.4 Magnetostrictive Materials

Magnetostriction is the deformation of a body in response to a change in its magnetic moment per unit volume (magnetization). Magnetization can be changed using an externally applied magnetic field or by changing the temperature. Figure 2.14 shows an example of magnetostriction wherein the length of the bar, L has changed by ΔL on increasing the magnetic field, H. Since this effect

was first discovered by Joule in 1842 in a bar of iron, the phenomenon has been named "Joule Magnetostriction" in his honor. Note that, almost all magnetic materials possess magnetostriction to some degree. However, giant magnetostriction is only observed for a small number of rare earth element containing materials.

Magnetostriction arises from the magnetoelastic coupling between classical properties of strain & elasticity and the intrinsically quantum mechanical & relativistic phenomena of magnetism. Magnetism is a result of an imbalance in the magnetic moments of a material's electrons. This imbalance can prompt the electrons to rearrange and produce a net magnetic moment in a particular direction. A by-product of this rearrangement is magnetostriction along with lowering of the crystal symmetry [86].

Magnetostriction can occur with (spontaneously) or without (non-spontaneously) the application of an external magnetic field. Large spontaneous magnetostriction occurs when a material is cooled below its Curie temperature. This is due to the phase transition from paramagnetic to ferromagnetic phase in the material. Non-spontaneous or forced magnetostriction occurs when saturation of Joule magnetostriction is achieved. Note that heating Curie temperature can lead to a loss of magnetostriction in the material.

2.4.1 History and Recent Developments

As mentioned earlier, Joule was the first to observe change in dimensions of an iron bar exposed to a magnetic field in 1842. Subsequent investigations revealed that polycrystalline nickel possessed largest Joule magnetostriction (– 40 ppm) with respect to other elements. Later in the 1860's, Villari discovered inverse magnetostrictive effect wherein an applied strain produced a change in magnetization of the material. Discovery of magnetostriction ultimately led to nickel and its alloys being widely used for military and civil applications in the late 1940's. Scope of such applications was however limited, because of the low magnetostriction in nickel, the material having known to possess highest magnetostriction at the time.

Search for materials with higher magnetostriction led to the discovery of large magnetostrictive effect (200 times that of Ni) in rare earth elements terbium (Tb) and dysprosium (Dy) in 1960s. However, the giant magnetostriction only existed at cryogenic temperatures and reduced to zero

at room temperatures due to their low Curie temperatures. Initial efforts in search for alloys with large magnetostriction and higher Curie temperatures focused on R_2Co_{17} compounds (R: rare earth element). These compounds were found to possess only moderate magnetostriction at room temperature [87].

Later efforts in this direction were focused on RFe_2 materials which were known to possess high Curie temperatures. Subsequently, it was revealed that Tb in RFe_2 form had a Curie temperature of ~ 700K and magnetostriction of the order of 2400 ppm at room temperature. However, large magnetic anisotropy in this material necessitated high magnetic drive fields to induce magnetostriction. To lower the magnetic anisotropy, Dy was introduced in the material which resulted in significant reduction in drive field. This composition had high magnetostriction, low drive fields and can be operated at room temperature. The material was later named Terfenol-D (**T**erbium Iron (**Fe**) **N**aval **O**rdnance **L**aboratory **D**ysprosium) in recognition of the lab where it was first synthesized [88–90].

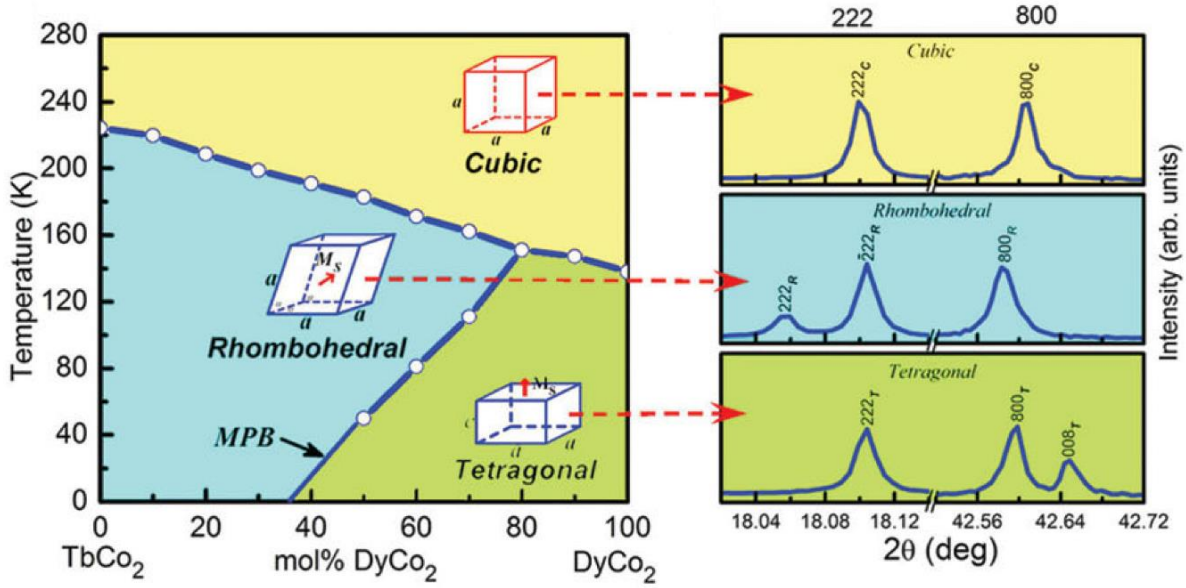

Figure 2.15 Phase diagram of TbCo2-DyCo2 (left) and synchrotron XRD profiles of different material phases (right) [91].

Terfenol-D has since become the most commercially important magnetostrictive material by capturing a large share in the magnetostrictive sensor and actuator market. More recently, the concept of a morphotropic phase boundary has been explored for magnetostrictive materials.

Analogous to piezoelectric materials, enhanced magnetostrictive properties were observed at the rhombohedral/tetragonal morphotropic phase boundary in TbCo2 – DyCo2 system around 160K temperature. The phase diagram and synchrotron XRD profiles of different material phases is shown in Figure 2.15.

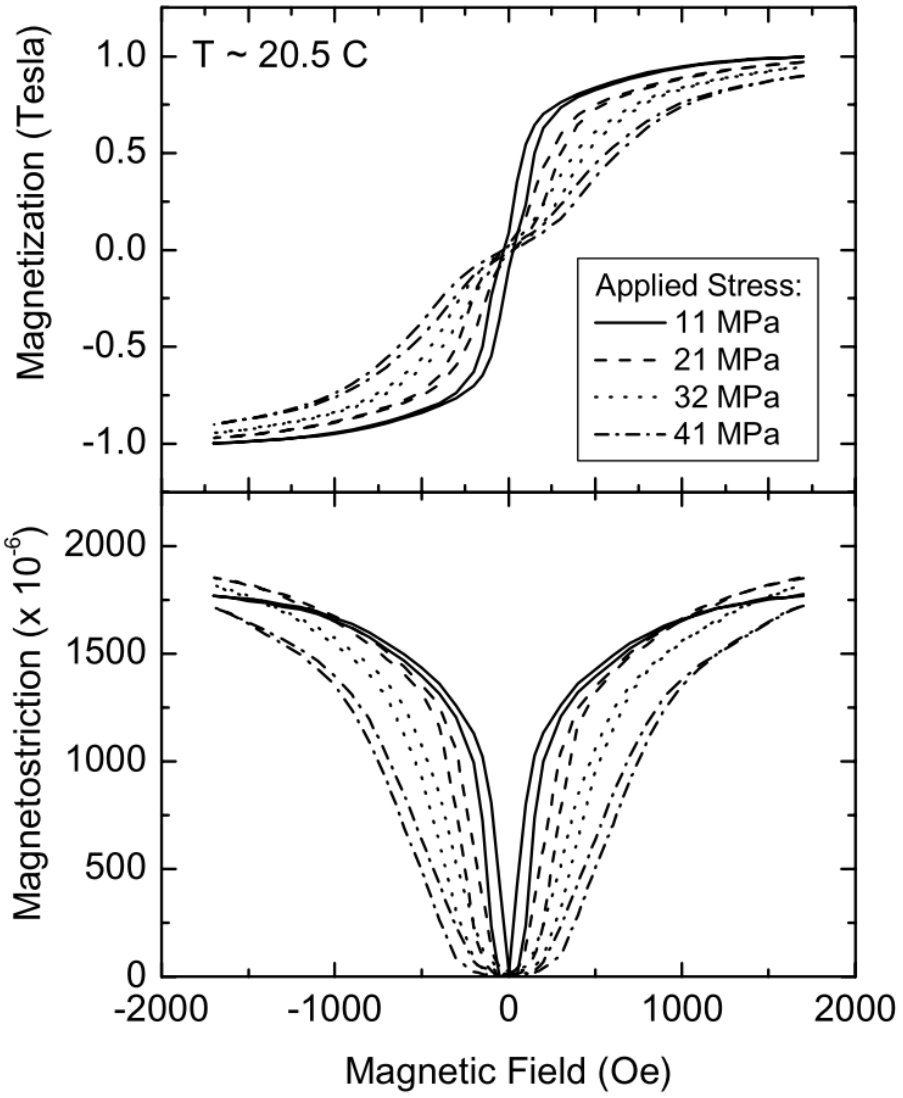

Figure 2.16 Magnetization and magnetostriction of Terfenol-D at T ~ 20.5 ℃[89].

2.4.2 Terfenol-D and Galfenol

Terfenol-D is usually denoted by $Tb_{1-x}Dy_xFe_2$ where the concentration at which room temperature magnetic anisotropy is minimized is $x = 0.7$. It solidifies in C15 cubic Laves phase with a unit cell consisting of two rare-earth and four transition-metal atoms. Since the magnetic anisotropy

depends on both composition as well as temperature, it is important to note that Terfenol-D possesses largest magnetization and magnetostriction only at room temperature (see Figure 2.16).

The crystallographic direction of the easy axis can change with temperature affecting the magnetic anisotropy in Terfenol-D which ultimately affects its magnetostriction. For example, at room temperature, Terfenol-D is present in the rhombohedral phase and the easy axis lies along $\langle 111 \rangle$ direction, resulting in largest magnetostriction. On the other hand, at low temperatures, a spin reorientation changes the easy axis from $\langle 111 \rangle$ to $\langle 100 \rangle$ direction along with crystallographic transformation to tetragonal phase reducing the magnetostriction magnitude by ~100ppm [87].

Change in magnetostriction can also be brought by changing the composition of terbium or dysprosium in $Tb_{1-x}Dy_xFe_2$ This is evident from the fact that easy axis at room temperature for x=0.73 lies along $\langle 111 \rangle$ direction whereas for $x > 0.8$, the spin reorientation changes the easy axis to $\langle 100 \rangle$ direction reducing the magnetostriction by an order of magnitude [90]. In an effort to improve magnetostrictive properties and reduce drive fields, Terfenol-D is often alloyed with other elements.

One such example is addition of holmium (Ho) in small quantities to replace either Tb or Dy in Terfenol-D. The composition is represented as $Tb_xDy_yHo_zFe_2$ and the result is a reduction in magnetic anisotropy which decreases required drive fields. Another example is the addition of cobalt (Co) to replace Fe in Terfenol-D. The composition is represented as $Tb_xDy_{1-x}(Fe_{1-y}Co_y)_2$ and results in increased anisotropy compensation temperature and Curie temperature. At x = 0.36 and y = 0.15, the composition is reported to possess giant magnetostriction with a wide temperature range of -80℃ to 100℃ [92, 93].

A substantial increase in magnetostrictive coefficient was reported in 2000 by alloying Fe with gallium (Ga) in small amounts [94]. This is interesting because Ga is non-magnetic in elemental form. The alloy with composition Fe_xGa_{1-x} is usually given the name Galfenol. Galfenol is relatively ductile and generally requires drive fields lesser than 32 kA/m to saturate magnetostriction. In contrast, Terfenol-D is brittle and requires drive fields an order of magnitude higher. A magnetostriction coefficient of 400 ppm has been successfully obtained for the

composition $Fe_{81}Ga_{19}$ by preserving the BCC $\alpha-$ Fe phase. Despite several attempts, the origin of large magnetostriction in Galfenol is still not completely clear. Table 2.5 provides properties of Terfenol-D and Galfenol for comparison.

Table 2.5 Magnetostrictive properties of Terfenol-D and Galfenol [89].

Property	**Terfenol-D**	**Galfenol**
Curie temperature, T_c	~ 700 K	~ 1000 K
Magnetization, $\mu_0 M_s$	1.0 T @300 K	1.7 T @300 K
Elastic Modulus, E	100 GPa @300 K	80 GPa @300 K
Saturation Magnetostriction, λ_s	2.0×10^{-3}@300 K	0.4×10^{-3}@300 K
Coupling Factor, $k_{\max}$	0.75 – 0.80	0.5 – 0.6
Mechanical Properties	Brittle	Tough
Useful Temperature Range	250 K – 525 K	0 K – 700 K

2.4.3 Comparison Between Magnetostrictive and Piezoelectric Materials

A summary of some fundamental differences between magnetostrictive and piezoelectric materials is given in Table 2.6.

Table 2.6 Comparison between magnetostrictive and piezoelectric material properties [95].

Magnetostrictive Materials	Piezoelectric Materials
• Inductive Materials • Actuator applications require moderate voltage (< 200V) & current (mA to A) • Low impedance • Eddy currents and hysteresis loss • Large strains possible (up to 2000 μ) • High coupling coefficient (0.70 – 0.75)	• Capacitive Materials • Actuator applications require high voltage (~ 1000V) at low current (mA) • Huge impedance • Leakage current • Limited strains (up to a 100 μ) • Low coupling coefficient (0.3 – 0.6)
• Non-contact configuration • Bonded configuration	• Always surface-bonded or embedded configuration
• Ductile	• Brittle
• Heavily nonlinear behavior, hard to model • DC magnetic bias or pre-stress required • High material cost	• Moderately nonlinear behavior, easy to model • Easy configuration • Low material cost

3. MANUFACTURING TECHNIQUES OF SMART MATERIALS

Since the manufacturing techniques and thermomechanical treatments performed on smart materials can influence their performance significantly, it is vital to discuss process parameters that correlate well with established figures of merit. The principle objective of any fabrication process is to produce a material with specified properties and do so repeatably with minimum variation and in an affordable manner. In this context, material properties will primarily be controlled by composition, however, other factors such as particle size, moisture content, process temperature/pressure or reactivity of raw material can play a significant role in determining properties of the finished product.

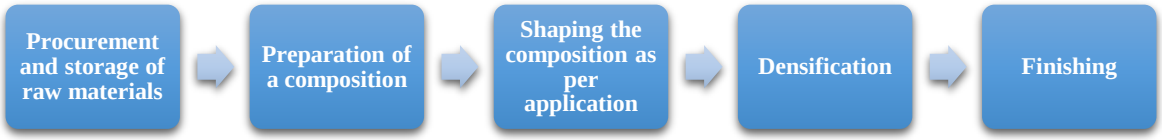

Figure 3.1 Major steps in manufacturing of a smart material.

The approach taken here is to elucidate manufacturing techniques for some of the most popular materials in each of the four subclasses i.e. piezoelectric materials, electrostrictive materials, shape memory alloys and magnetostrictive materials. This is done in the hopes of revealing similarities between process parameters across subclasses that appear to govern material properties. In cases where a manufacturing technique is used for more than one subclass, emphasis is placed on the process parameters that differ from one subclass to the other. In general, any fabrication process can be broadly divided into five distinct stages (Figure 3.1).

The first step is procurement and storage of raw materials. To ensure repeatability, it is paramount that raw materials are procured according to specifications of the fabrication process, properly catalogued and, stored. Next step is to promote conversion of raw materials to a desired composition. In case of ceramics, this is usually performed by oxide-mixing technique in which raw oxide powders are fired for several hours at elevated temperatures (calcination or pre-sintering) and crushed into fine powder. Once a desired composition is obtained, the powder is compacted to final or near final shape.

The agglomerate is then fired at high temperature to diffuse atoms, promote grain growth and increased density. This firing process is also called sintering. Finally, any burrs or additional features are machined-off of the sintered agglomerate. Note that all steps may not be required in some cases and additional steps may be incorporated to serve the needs of a specific application [96]. Before we begin our discussion, it is important to classify the manufacturing techniques based on a pre-selected criterion.

Classification of materials can be done using a variety of criteria based on state: liquid, solid, gas; phase: polycrystalline, single crystal; material type: metals, non-metals, ceramics; form: thin film, bulk material etc. Classification of manufacturing techniques utilized here follows a similar trend. At the top level, the classification of materials starts with material phase (polycrystalline, single crystal). The polycrystalline materials further branch out based on the processing stage the material is in, for example, powder preparation can be done using solid-state reaction technique, coprecipitation technique etc. Some of the stages like shaping is further classified into bulk or thin films based on the final shape of the processed material. Interestingly enough, thin films can be fabricated using any of the solid, liquid or gas/vapor phase manufacturing processes as per requirement (Figure 3.2). The fabrication process of the most commonly utilized piezoelectric material (PZT) is discussed next.

PZT is fabricated in various shapes, sizes and composition depending upon the final application. For a particular application, the shape and material composition, including any dopants in case of PZT, is finalized even before production depending upon the form/fit and phase transitions governing material properties. The manufacturing process begins with mixing of raw materials (PbO, TiO_2, ZrO_2) precisely weighted to ensure a morphotropic composition and dopants such as Barium (Ba), Lanthanum (La), Niobium (Nb), Strontium (Sr), Antimony (Sb), and Iron (Fe) oxides. Dopant selection is made depending upon whether a hard or soft PZT is required. Subsequent mixing of raw materials is usually done by wet-ball milling.

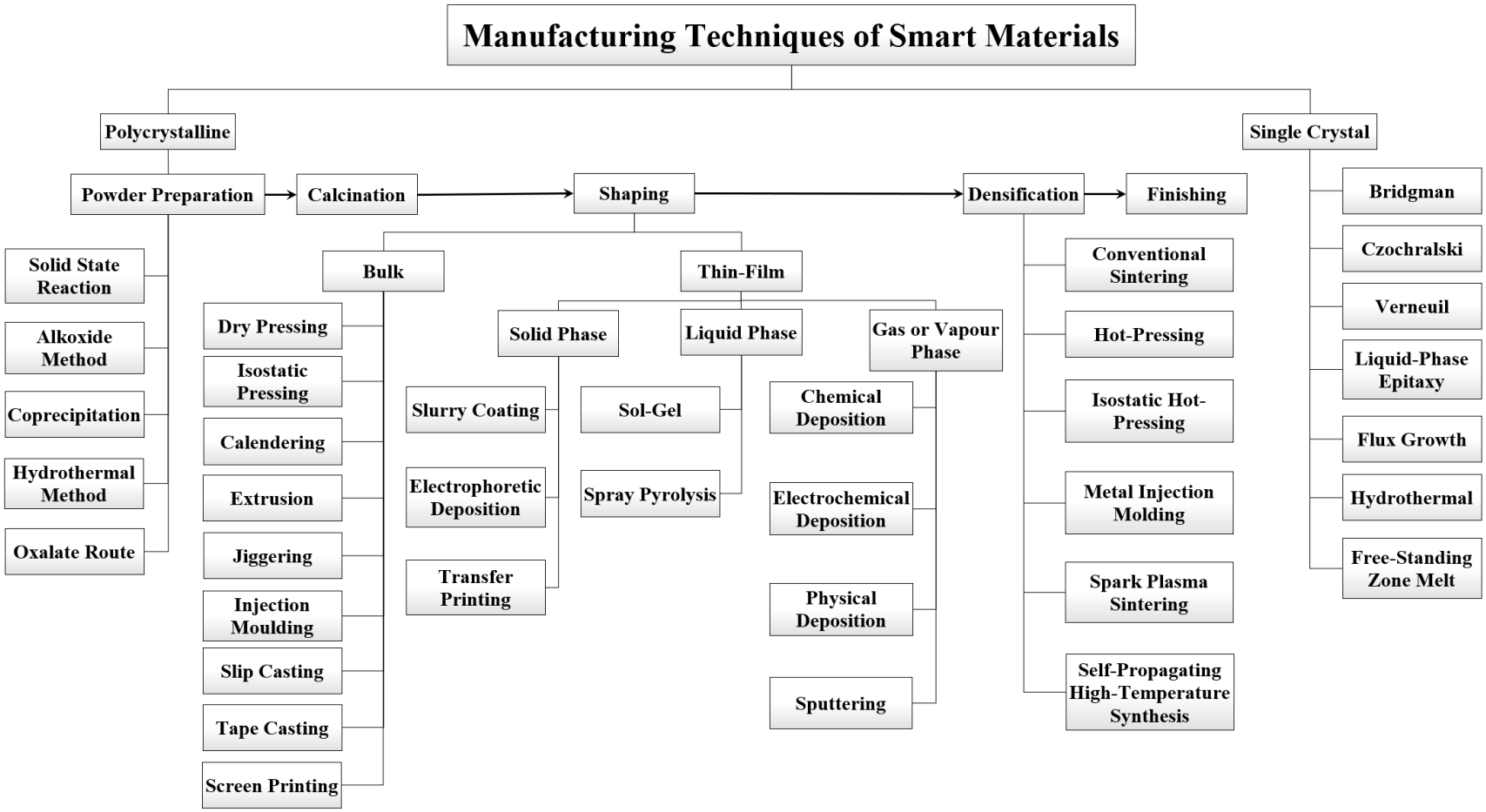

Figure 3.2 Manufacturing techniques of smart materials [13, 14, 17, 96, 97].

The process parameters for wet-ball milling are given in Table 3.1.

Table 3.1 Wet ball-milling process parameters

Parameter	**Typical Value**
Volume of milling media (balls)	~ 3 times volume of milled material
Volume of liquid (water)	1 – 2 times volume of milled material
Largest diameter of ball	~ one-tenth of the milling barrel diameter
Rotation rate of mill	300 – 400 rpm
Milling time	5 – 480 min.
Final Particle size	1 – 10 µm

After mixing of the raw materials, spray drying is performed to evaporate water and prepare the material for calcination. In spray drying, the process slurry is pumped at high pressure through a small nozzle which promotes atomization into smaller particles. These particles are carried by hot air through the dryer and get discharged as a dry powder at the bottom of the chamber. A successful spray drying operation necessitates careful control of process parameters such as temperature, pressure, airflow, slurry flow and the volume of the slurry entering the dryer.

The dry powder is then calcined to promote inter-diffusion of ions and reduce the amount of diffusion that must occur during sintering. It is usually performed in air atmosphere at temperatures of about 900 – 1000 ℃ for a period of 1 – 2 hours. High purity crucibles are used for calcination to limit contamination. The calcination conditions control the amount of shrinkage during sintering and need to be properly regulated to yield a consistent product. After calcination, a liquid binder solution necessary for shaping is added.

Further, to break agglomerates and reduce size of the particles, the material is wet-milled again followed by spray drying. This is essential because agglomerates densify more rapidly internally rather than with neighboring agglomerates resulting in residual pores. The small size of particles is desirable as the time taken for neighboring particles to inter-diffuse is known to be proportional

to the square of particle size. A free-flowing binder containing powder with narrow agglomerate size distribution is obtained at this point. Parameters such as morphology, particle size, binder content, and moisture content of the dried material are important factors for shaping which is the next step.

Shaping the material into a partially dense green bodies (~ 60% dense) can be done by a number of methods such as isostatic pressing (dry or wet), single-action uniaxial, dual-action uniaxial or rotary uniaxial presses. Commercially, PZT powder is shaped into near final shapes using uniaxial pressing due to its simplicity and cost-effectiveness. Control of parameters such as powder particle size, compaction ratio, die/punch clearance, compaction pressure, pressing speed, die friction and parts per minute are essential to ensure success of the shaping process and prepare the part for binder burn out and sintering.

As mentioned earlier, binder material is added after calcination for ensuring material cohesiveness during the shaping process. The process of removing these binders after pressing via combustion (air atmosphere) or pyrolysis (nitrogen atmosphere) is called binder burn out. Most commonly used binder materials are polyvinyl alcohol (PVA) and polyvinyl butyral (PVB). The molecular weight of the binder material along with its behavior in the PZT component under an applied stress control the quality of PZT component. The binder burn out profile (temperature vs time) is an important design parameter as the byproducts can cause micro-cracking or mechanical failure of the component unless released by diffusion through open pores. Before we discuss any further, note that the overall PZT manufacturing process is summarized in Figure 3.3 with a flow chart.

After binder burn out, densification is performed by sintering the component at a temperature range of 1000 – 1300 ℃. The driving force for densification of the material is reduction in overall surface area which reduces the free energy of the material. Soaking times at peak temperature for the material vary from 2 – 6 hours which lead to a theoretical density > 95% and low porosity. Note that evaporation of lead oxide can be issue since it evaporates around ~ 800℃. To combat this, sealed alumina crucibles or a lead atmosphere is often employed. Other parameters such as cooling rate, component size and geometry, component shrinkage also play an important role in quality of sintered ceramic.

Machining the sintered component using an abrasive comes next with surface finish of the PZT component being the most important characteristic. Successful machining operation requires a compromise between tool wear rate, feed rate of PZT into the abrasive and surface speed of the abrasive. Typical values are given in Table 3.2.

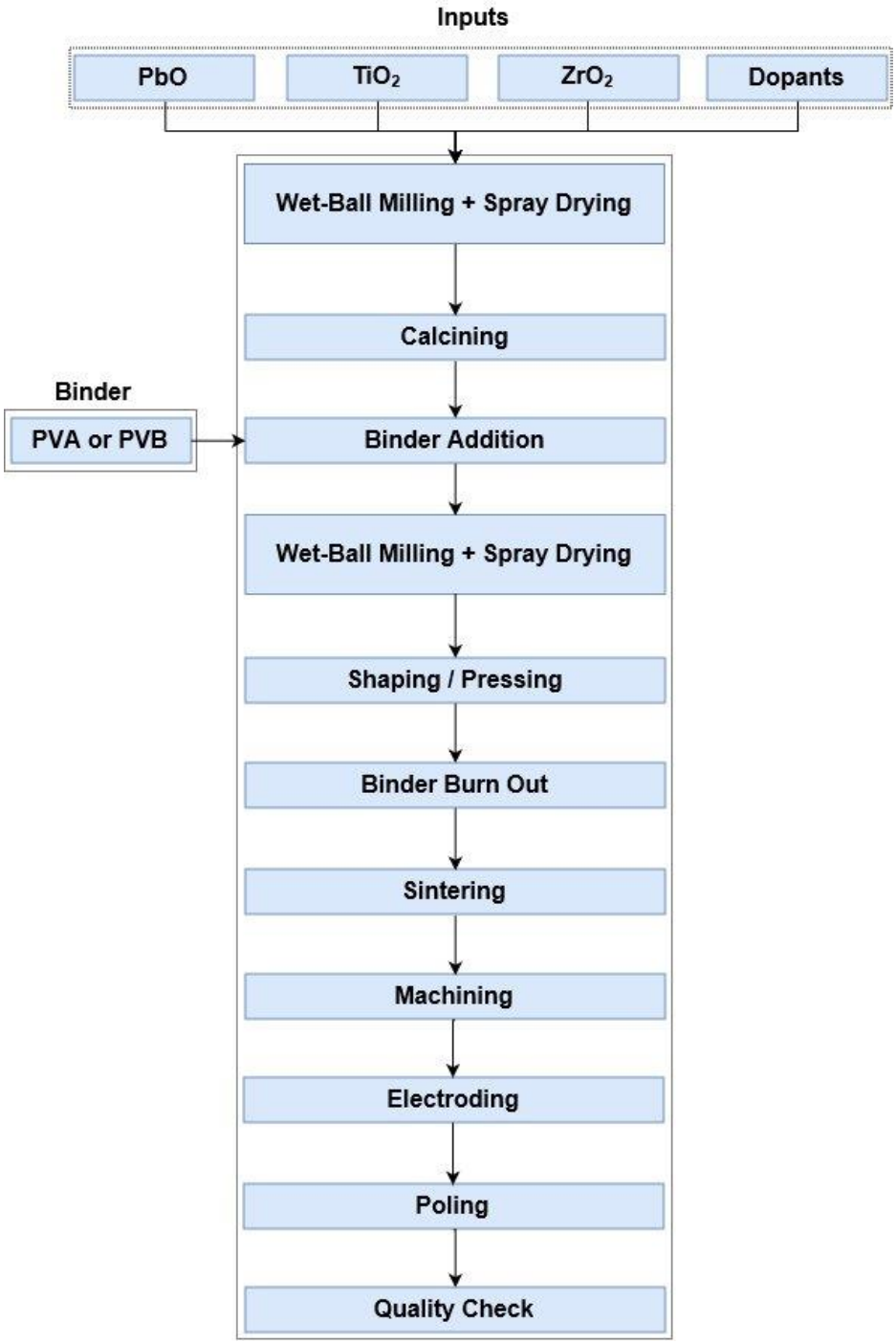

Figure 3.3 Commercial PZT manufacturing process.

Table 3.2 Machining parameters for PZT manufacturing.

Parameter	Typical Value
Abrasive material	320 grit diamond
Surface finish	$R_a < 0.7$ μm
Surface speed	1200 – 1800 meters / min
Feed rate	25 – 200 mm / min

Electroding the component is accomplished via screen printing process due to its simplicity, low cost and flexibility in shapes that can be electroded. A paste containing around 70 – 75 % silver, 20 % organic binders and 5 % glass (required for bonding silver to ceramic surface), is applied on the machined PZT surface either manually or automatically. After application, dry air is circulated followed by oven dry at 125 °C. This process is repeated on the other side as well ensuring a stable layer of silver electrode on both sides. Subsequent firing at higher temperatures (~ 500 – 850 °C) ensures evacuation of binders and penetration of glass into the ceramic substrate.

Poling is performed next at high electric field, temperature less than Curie temperature and for a sufficient amount of time which results in realignment of the domains and net overall polarization. The success of poling can be measured by d_{33} and the difference between resonance and anti-resonance frequencies measured using an impedance analyzer. A quality check is finally performed to ascertain whether the manufactured component meets requirements such as d_{33}, resonant frequency, anti-resonant frequency, capacitance etc.

4. PROPOSED APPROACH FOR PROPERTY ENHANCEMENT

As discussed earlier, manufacturing techniques of smart materials consist of a number of individual operations that lead to the final product / device. These sublevel operations make up an overall process chain in which several parameters interact with each other in a non – linear manner and influence the final performance / quality of the material. The physical phenomena governing most these interactions are difficult to model analytically due to a large number of parameters and presence of inherent non – linearity. In such cases, an alternate approach capable of modeling complex non – linear behaviors is desired.

Artificial neural networks have been historically successful in mathematically mimicking a wide range of complex non – linear physical phenomena. A number of successful implementations for modeling a single process in a manufacturing process chain have been reported. However, the prospect of process chain optimization as a whole for property enhancement of smart materials hasn't been reported to author's knowledge. A first approach to process chain modeling for a manufacturing technique would be to provide inputs for all the stages at the start of the artificial neural network and use the final figure of merits as outputs.

This approach is flawed because it doesn't accurately model the physical process in that the processes have a hierarchical structure between themselves. The outputs from one process stage influence the performance of next stage along with the parameter settings governing it. This means the artificial neural network has to figure out the inherent structure based on data which increases the amount of data and computational cost required. In order to address these issues, a paradigm of hierarchical modeling of manufacturing process chains using artificial neural networks for property enhancement has been introduced here. The typical issues of data collection, data preprocessing, identification of input parameters etc. associated with artificial neural network modeling, to achieve a favorable outcome, are also briefly addressed.

In what follows, a novel artificial neural architecture for hierarchical modeling of manufacturing techniques and property enhancement has been proposed. This is accompanied with a discussion on the challenges behind some of the more common approaches for process modeling and how the proposed architecture hopes to address those. The mathematics and detailed steps to train and test the network are also provided. It is the author's belief that using this framework in combination

with an evolutionary optimization paradigm such as genetic algorithm can modestly yield incremental improvements in figure of merit at a fraction of the costs and time involved in new materials discovery.

4.1 Hierarchical Process Modeling using Artificial Neural Networks

If we assume the manufacturing process chain to be serial *i.e.* there is no converging / diverging material flow, it can be viewed as consisting of a number of individual process stages. Each of these individual process stages receives some input parameters (P_i) that we control and the output parameters / quality characteristics (S_{i-1}) from the previous stage. The process stage then produces output parameters (S_i) using this combined input information. So, if we have a way to accurately model individual process stages, we can use a linear combination of individual artificial neural networks for each of the individual process stages and model the entire process. How this would look in practice is given in Figure 4.1. Note that for the i^{th} process stage, artificial neural networks can be trained using input process parameters (P_i , S_{i-1}) and output quality characteristics (S_i).

On the outset this seems to be a manageable problem with artificial neural networks. We have input parameters ($i_1, i_2, \ldots, i_j$) going into a non-linear physical process and output parameters ($o_1, o_2, \ldots, o_l$) from the individual process stages. However, there are several challenges to this. These are outlined below:

- Output from individual process stages may not always be measurable. In case of PZT manufacturing for example, powder morphology after a milling operation is difficult to measure.

- Most of times, we are not definitively sure about what all the output characteristics (in the process modeling context) from an individual process stage are.

- The network architecture doesn't accurately model the physical process in that the input from first architecture has no bearing on subsequent processes directly. This means a larger artificial neural network is required to model individual processes to capture the intrinsic relationship between subsequent processes increasing computational cost.

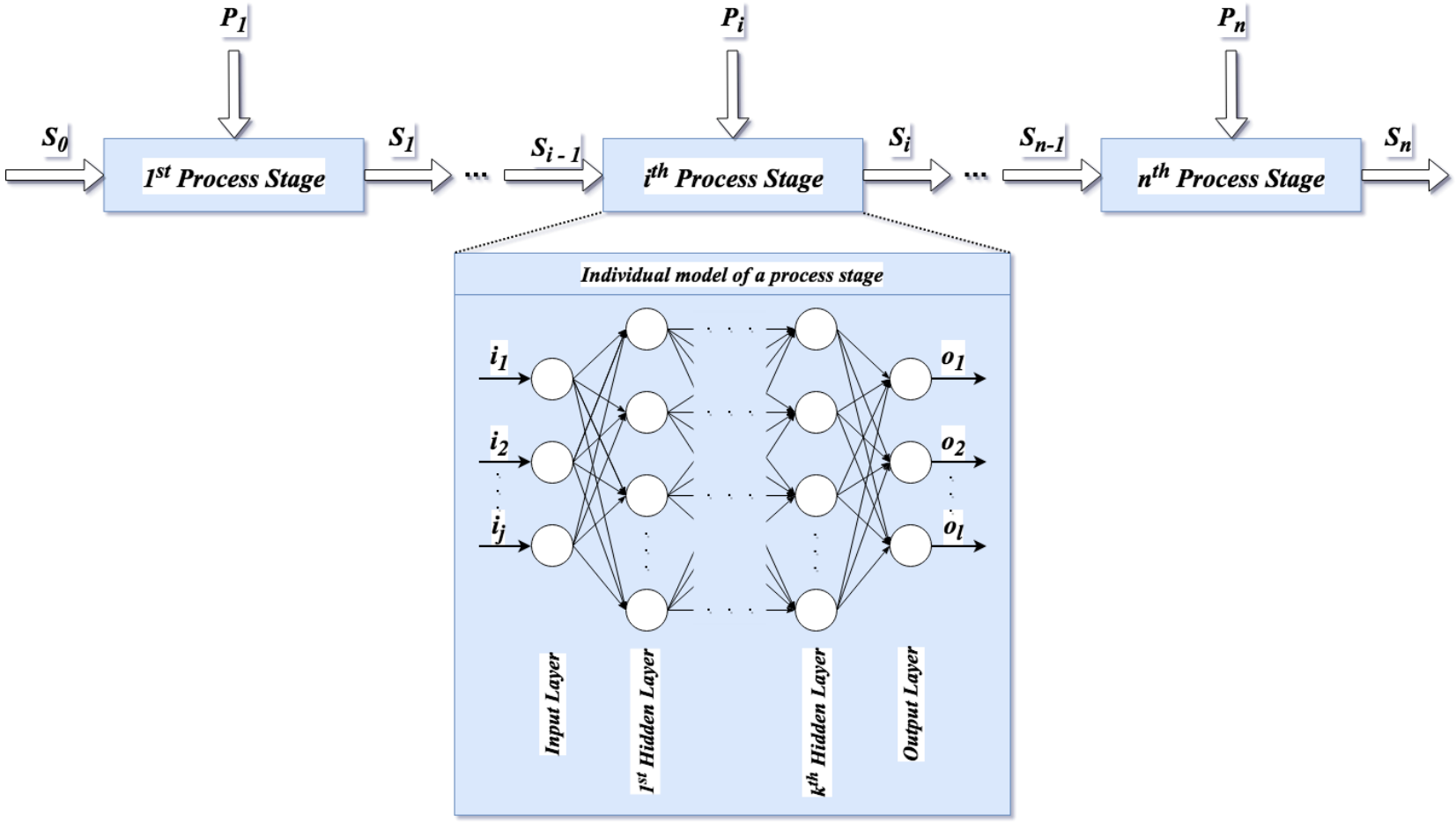

Figure 4.1 Manufacturing Process Model using Linear Combination of Artificial Neural Networks.

As mentioned earlier, there are a number of disadvantages in using the network architecture given in Figure 4.1 for manufacturing process modeling. In order to alleviate these issues, a novel artificial neural network architecture has been proposed (See Figure 4.2). In this network, the first layer consists of inputs for the first stage and the inputs for the second stage are fed (along with the outputs of the first hidden layer) as inputs to the next hidden layer. The subsequent hidden layers are fed inputs for the subsequent stages along with the outputs of the hidden layer immediately preceding them. Finally, fully connected layers are added just before the output layer.

The proposed artificial neural network architecture addresses the issues mentioned earlier as follows:

- Outputs from individual stages do not need to be explicitly specified since the outputs from a previous stage are directly fed to the next layer along with the inputs for that particular process stage. The number of neurons in the hidden layers can be manipulated / controlled based on the level of understanding about a particular process stage (since, each neuron in a hidden layer is thought to be representing an output variable for a process stage).

- The knowledge about all the outputs required for describing an individual process stage is not required. This is because varying the number of neurons in the hidden layer gives control over individual process stage behaviors in the overall process chain model.

- Most importantly, the artificial neural network architecture is setup in a hierarchical manner representative of the actual physical process. This means while training the network doesn't need to figure out the inherent process structure of the manufacturing technique from the data. In other words, comparatively lesser data and computational cost would be required than a traditional multilayered feedforward artificial neural network architecture.

In the sections that follow, each of components essential in data collection, preprocessing, training & testing and the mathematics behind the training process is discussed in detail. It is the author's hope that the proposed artificial neural architecture along with real world data of a manufacturing process can be beneficial for a variety of applications contingent on process modeling.

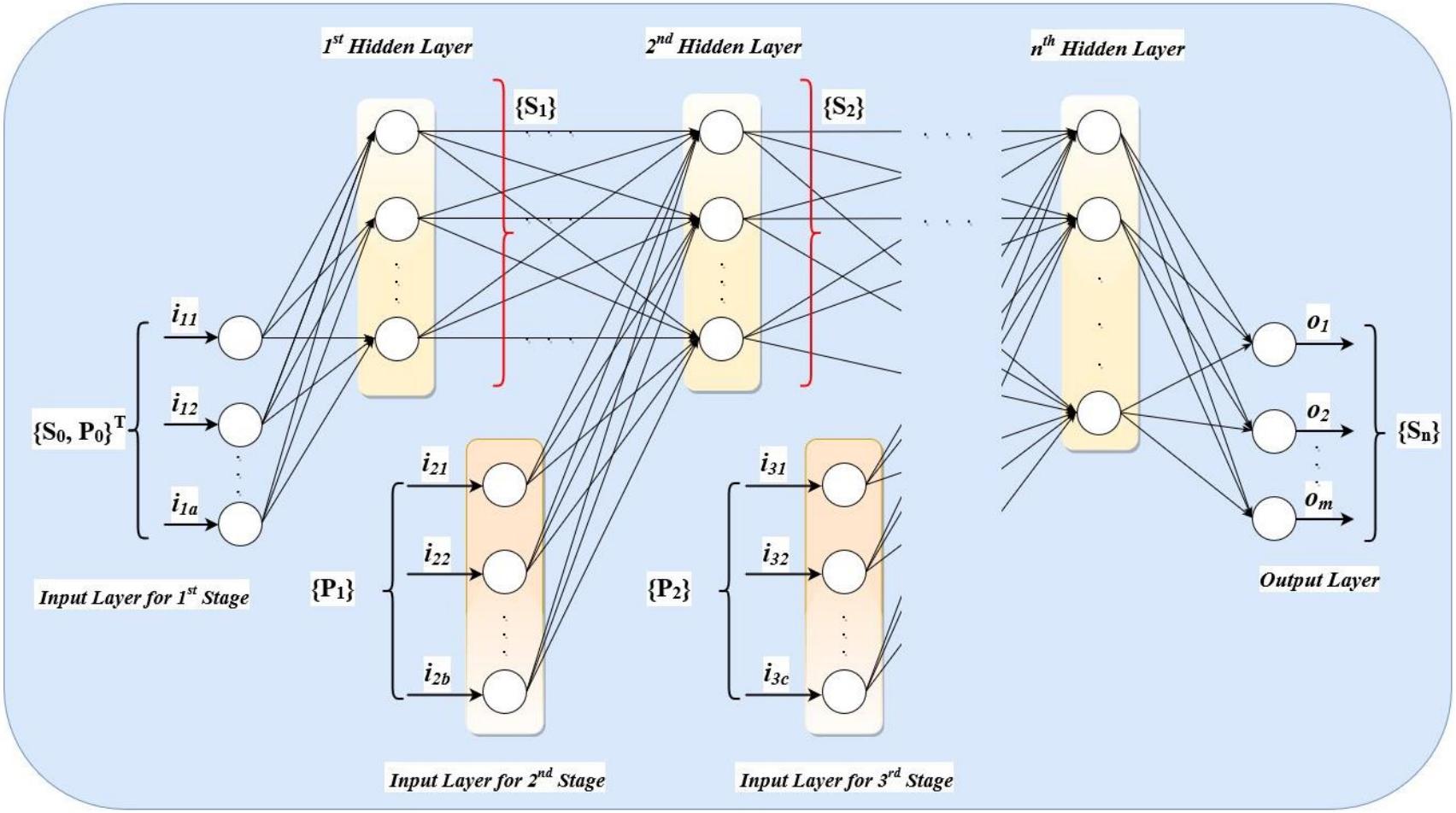

Figure 4.2 Hierarchical Model of a Manufacturing Process Chain.

4.1.1 Identification of Input Parameters for Individual Process Stage

The first step towards manufacturing process modeling is identification of input process parameters for each individual stage of the process chain. The input parameters are associated with things that are under our control, meaning the values of which we can modify. Figure 4.3 presents a flow chart for commercial PZT manufacturing process along with the parameters affecting figure of merit and is a good way to document input parameters before beginning actual training process.

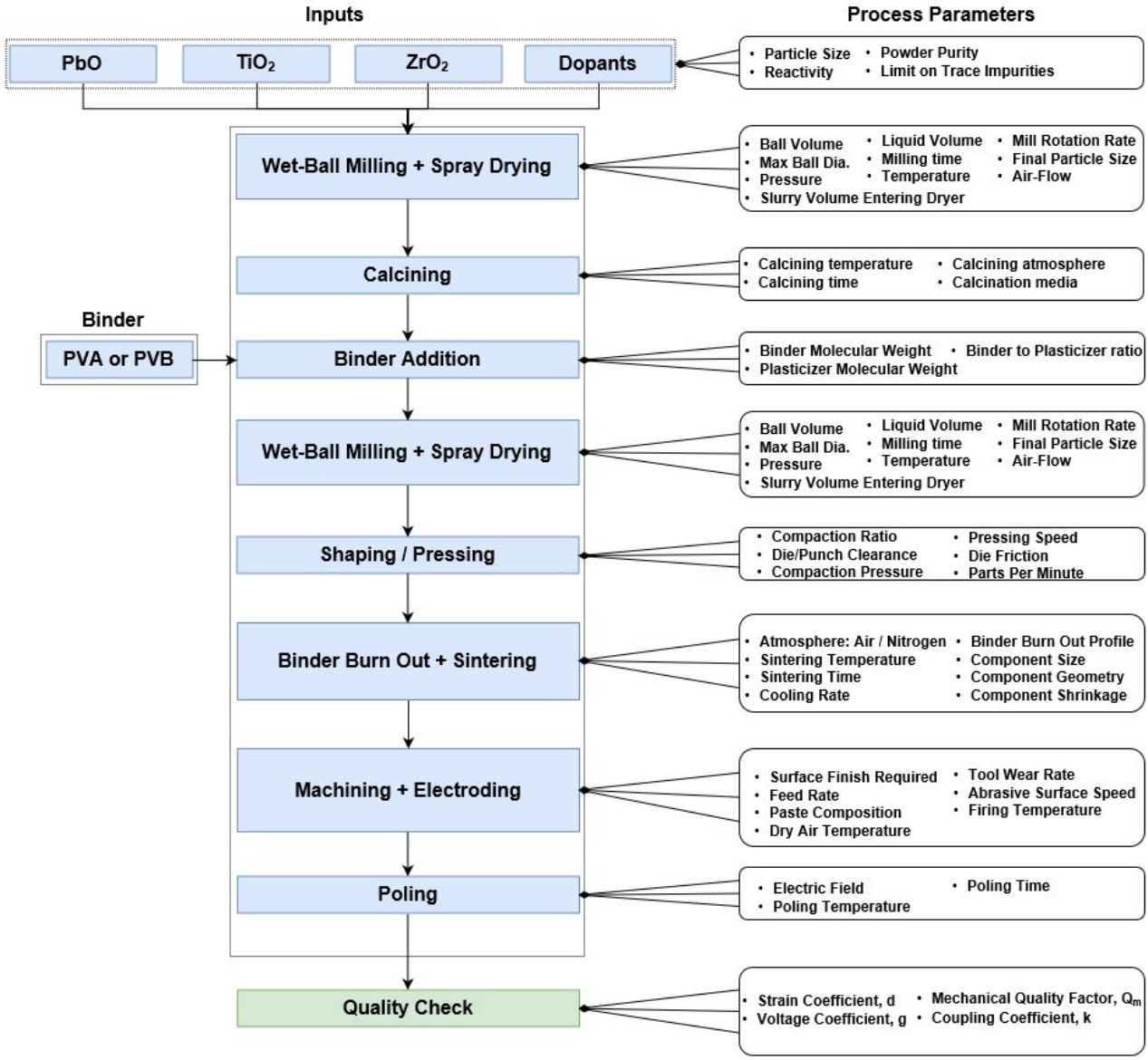

Figure 4.3 Commercial PZT manufacturing process with parameters affecting figures of merit [13, 14, 17, 96, 97].

4.1.2 Data Collection

The amount of training data required is contingent on many factors of the cumulative manufacturing process. The volume of training data is critical to estimating the number of records to be imported from an experimental space of process parameters. It further determines the number of training samples required to achieve a desired level of model performance. This would lend to an effective comparison of efficiencies between different proposed architectures. The amount of data required for a particular architecture would depend on the unknown underlying mapping functions that could best define a correlation between input variables to the output variable(s). In addition, it would also depend on the algorithm used to learn the unknown mapping function from the training data. From a learning curve, it would then be possible to project the amount of data that is required to develop an optimized model which minimizes the requisite data without hitting an inflection point of diminishing returns.

4.1.3 Data Preprocessing

At the heart of artificial neural networks, numerical optimization algorithms such as gradient descent for example, have to balance exploration and exploitation of the search space to tune the weights and biases of the network. More often than not, the data fed into the artificial neural network has to be reconditioned in order for this tuning to happen effectively. This data reconditioning process can involve:

a. Elimination of outliers from the dataset: Outliers may be generated due to variable measurements or by intrinsic experimental error. This can mislead the training process resulting in longer training times, less accurate models and, ultimately, poorer results. Common methods to counter the effect of outliers include the univariate method which searches for extreme values of one variable in data points and the multivariate method which searches for unusual combinations of all variables in data points [98].

b. Linear scaling or statistical normalization of input data: Scaling or normalization is done to ensure that all features are in a comparable range. While scaling is not a functional requirement for the artificial neural networks to learn, it helps considerably by transposing the input variables into the data range of activation functions. For example, in the range [-1, 1] for

sigmoid activation function. Some common normalization approach utilized include statistical normalization (using mean and standard deviation) and min-max scaling.

c. Dimensionality reduction could be employed to save computational cost while retaining prediction accuracy by reducing the number of random variables under consideration. This would help in data compression and removal of redundant features. This is done by obtaining sets of principal variables through feature selection or feature extraction [99]. Some methods include:

i) Variable Selection via Correlation Quantification
ii) Clustering
iii) Principal Component Analysis (PCA)
iv) Independent Component Analysis (ICA)

4.1.4 Training the Proposed Network

The core of training a traditional artificial neural network involves the backpropagation algorithm [100–102] with a predefined cost function (usually mean squared estimate). The algorithm provides a framework on how to propagate the error (between the true output and the output generated by the network for the current example) back into the network. This is done in order to tweak the weights and biases of individual neurons so as to ultimately minimize the cost function. Doing this for a certain number of training examples results in a set of weights and biases which can estimate the non – linear relations between the input and output fairly well.

In order to train the proposed artificial neural network architecture, the backpropagation algorithm needs to be rewritten in such a way that the error from the output neurons can be used to tune weights and biases for the input layers for the later stages of the manufacturing process chain (refer Figure 4.2). The modified formulation of the backpropagation algorithm for the proposed artificial neural network architecture is presented. The first step in training of the proposed artificial neural network is to calculate the output layer error using,

$$\delta^L = \Delta_a C \odot \sigma'(z^L) \tag{4.1}$$

Once the output error is calculated, it is propagated back to the inner layers using the recursive relation,

$$\delta^l = ((w^{l+1})^T \delta^{l+1}) \odot \sigma'(z^l) \tag{4.2}$$

Finally, the biases and weights are tweaked using the propagated error information via Eq. (4.3) and Eq. (4.4).

$$\frac{\partial C}{\partial b_j^l} = \delta_j^l \tag{4.3}$$

$$\begin{aligned} \frac{\partial C}{\partial w_{jk}^l} &= a_k^{l-1}\delta_j^l \\ \frac{\partial C}{\partial w_{jk}^{lip}} &= a_k^{lip-1}\delta_j^{lip} \end{aligned} \tag{4.4}$$

Table 4.1 Hyperparameters for Python implementations.

Property	Traditional ANN	Cascaded ANN
Batch size	50	50
Learning rate	0,5	0,5
Number of epochs	20	20
Number of hidden layers	2	2
Number of neurons in each hidden layer	3	3
Total number of layers	4	5 (inputs split in 2 layers)
Total number of inputs to the network	3	3
Total number of outputs from the network	1	1

The notations utilized are standard as in [102] except for subscript "*lip*" which is used to refer to the l^{th} input layers. '$\odot$' is the symbol for Hadamard or Schur product. Due to difficulty in obtaining actual experimental data from an industrial manufacturing process, the validity/convergence of this approach is tested using artificially generated data and Python implementations with a small number of neurons. The hyperparameters for both traditional as well cascaded artificial neural networks were kept identical to compare their performances and are given in Table 4.1. Moreover, the seed for random number generator in Python was kept the same for both implementations. The functions used to generate artificial data (Matyas function [103]

and McCormick function [104]) are plotted in Figure 4.4. As it can be seen, these are highly non-linear and a challenge for the relatively simple Python implementations considered here.

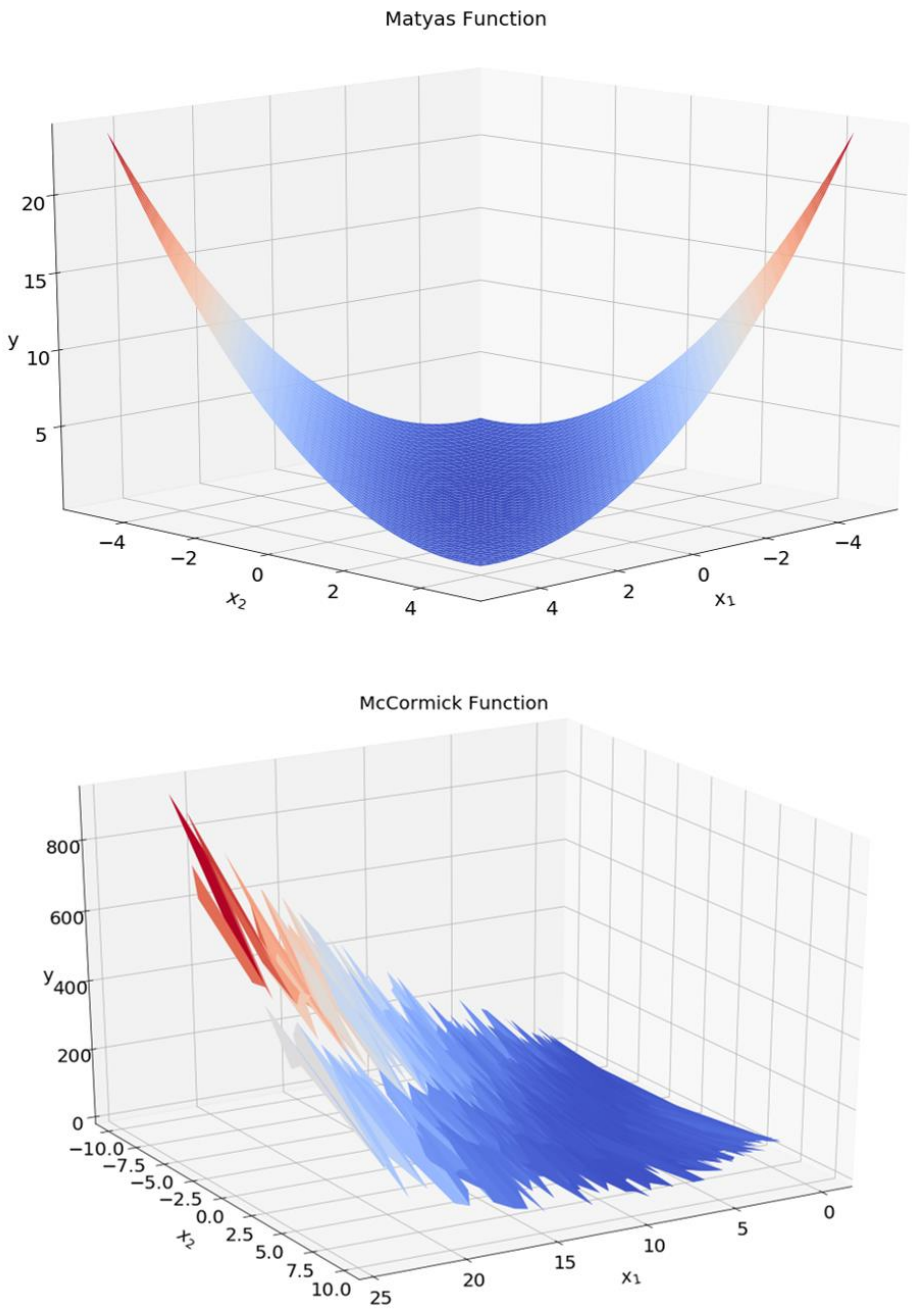

Figure 4.4 Nonlinear functions used to generate artificial data.

The traditional and cascaded artificial neural network architectures utilized for the implementations are given in Figure 4.5.

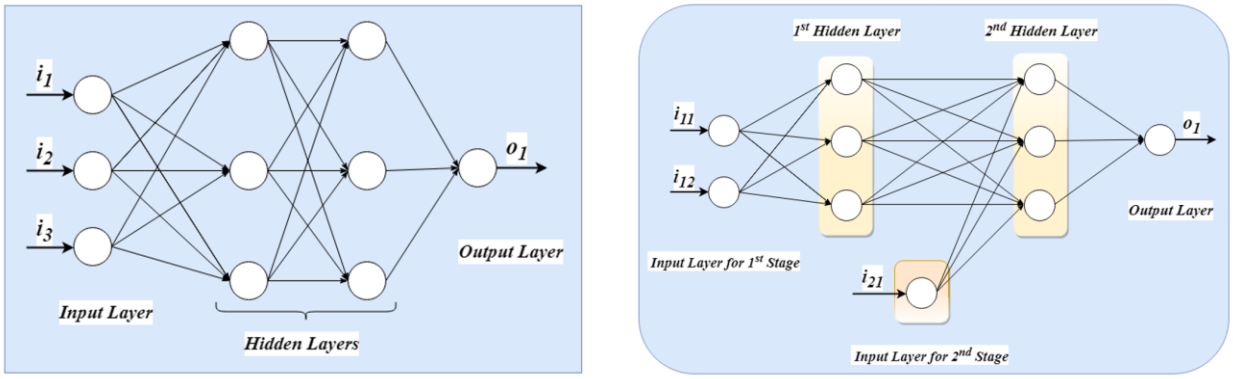

Figure 4.5 Architecture for traditional (left) and cascaded (right) artificial neural networks used for Python implementations.

Based on the mathematical formulation performed earlier, the CANN is trained and mean squared error is monitored as the training progresses over 20 epochs. The same is done for the traditional ANN and progress is compared in Figure 4.6. It can be observed that CANN architecture is converging incrementally faster than the traditional ANN architecture. The code for the Python implementations can be found on github [105].

```
Epoch 0: 9423.52219476
Epoch 1: 9423.50872557
Epoch 2: 9423.50346281
Epoch 3: 9423.50066883
Epoch 4: 9423.49893926
Epoch 5: 9423.49776358
Epoch 6: 9423.49691258
Epoch 7: 9423.49626796
Epoch 8: 9423.49576294
Epoch 9: 9423.49535639
Epoch 10: 9423.49502214
Epoch 11: 9423.49474251
Epoch 12: 9423.4945051
Epoch 13: 9423.49430101
Epoch 14: 9423.49412371
Epoch 15: 9423.49396823
Epoch 16: 9423.49383081
Epoch 17: 9423.49370844
Epoch 18: 9423.49359879
Epoch 19: 9423.49349999
```

```
Epoch 0: 9423.50449076
Epoch 1: 9423.49998102
Epoch 2: 9423.49792806
Epoch 3: 9423.49670797
Epoch 4: 9423.49590818
Epoch 5: 9423.49532227
Epoch 6: 9423.49488234
Epoch 7: 9423.4945375
Epoch 8: 9423.49425742
Epoch 9: 9423.49402662
Epoch 10: 9423.49383437
Epoch 11: 9423.49367022
Epoch 12: 9423.49352975
Epoch 13: 9423.49340753
Epoch 14: 9423.49330017
Epoch 15: 9423.49320527
Epoch 16: 9423.49312089
Epoch 17: 9423.49304513
Epoch 18: 9423.49297685
Epoch 19: 9423.49291501
```

Figure 4.6 Mean squared error for traditional (left) and cascaded artificial neural network (right) as the training progresses.

4.2 Optimization for Property Enhancement

The property enhancement approach described here begins with identification of the input parameters associated with individual process stages in a manufacturing process chain and the final quality / figure of merit parameters of the finished product / device. For example, for the sintering process inputs include sintering time, temperature, pressure, particle size etc. Similarly, outputs can be density, yield strength or piezoelectric coefficient in case of piezoelectric materials and so on. The next step is to gather production run data (manufacturing dataset) for the process in question using a data collection strategy. The raw data needs to be preprocessed before it can be used for training the artificial neural network.

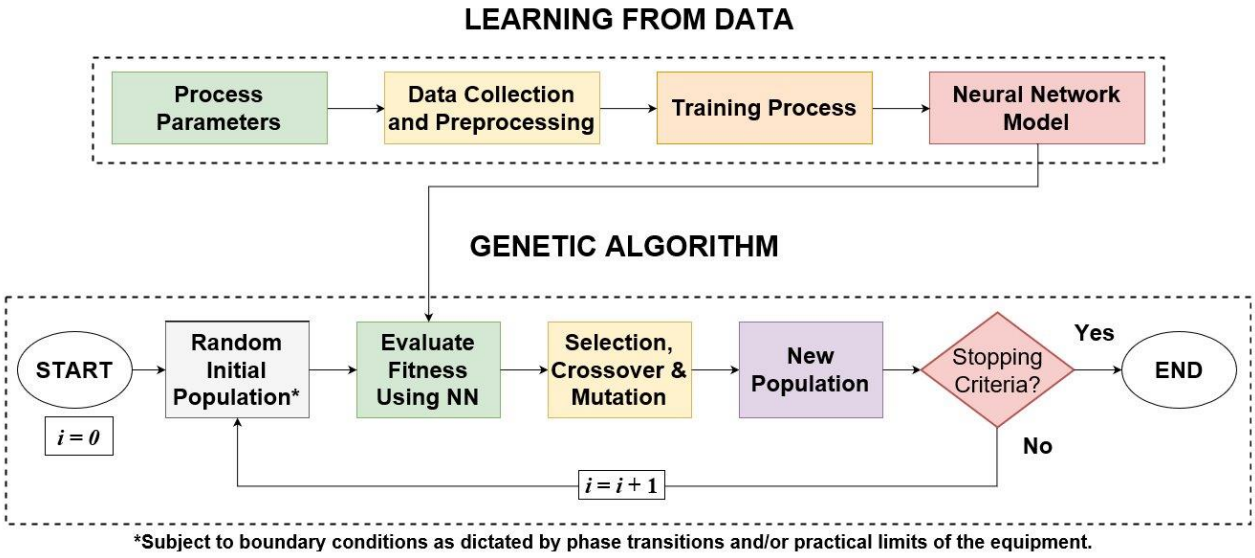

Figure 4.7 Genetic algorithm for property enhancement.

The process dataset is then split in to training, validation & test data and an artificial neural network is trained using the methodology suggested in the previous section. Once a reasonable test set accuracy is established, it is assumed that the artificial neural network has adequately captured the physical phenomenon from data (learning from data). This may require tuning the hyperparameters and several iterations before an acceptable model is obtained. The next step is to actually utilize the trained artificial neural network model for property enhancement. This is accomplished with an optimization algorithm by varying the input parameters to the artificial neural network model and observing the output figure of merits.

The search for an optimum set of input process parameters needs to balance exploration and exploitation of the search space. Random Monte Carlo simulation can work for a problem with less number of input and output dimensions. However, as the problems become increasingly non-linear, an optimization algorithm that can effectively navigate local minima is needed. In such cases, a heuristic global evolutionary optimization technique such as genetic algorithm can be utilized to fine tune the search. The schematic of genetic algorithm is given in Figure 4.7. Note that the artificial neural network model will serve as a black – box function for the fitness evaluation step in the optimization algorithm.

5. SUMMARY, CONCLUSIONS AND FUTURE WORK

A novel cascaded artificial neural network architecture for hierarchical modeling of the manufacturing processes of smart materials was proposed. The mathematics behind the training process and modification in the backpropagation algorithm was reported and the approach was validated using a simple Python implementation on artificially generated data. By coupling the trained artificial neural network architecture with an evolutionary optimization algorithm such as genetic algorithm, a framework for property enhancement of smart materials was also presented. Future work will involve collaboration with a smart materials manufacturer to test the validity of the proposed approach on real data with a more refined implementation of CANN architecture.

REFERENCES

[1] D.J. Hartl and D.C. Lagoudas, “Aerospace applications of shape memory alloys.,” *Journal of Aerospace Engineering*. vol. 221, no. 4, pp. 535–552, 2007.

[2] O.E. Ozbulut, S. Hurlebaus, and R. Desroches, “Seismic response control using shape memory alloys: A review.,” *Journal of Intelligent Material Systems and Structures*. vol. 22, no. 14, pp. 1531–1549, 2011.

[3] G. Song, N. Ma, and H.N. Li, “Applications of shape memory alloys in civil structures.,” *Engineering Structures*. vol. 28, no. 9, pp. 1266–1274, 2006.

[4] F. El Feninat, G. Laroche, M. Fiset, and D. Mantovani, “Shape memory materials for biomedical applications.,” *Advanced Engineering Materials*. vol. 4, no. 3, pp. 91–104, 2002.

[5] T. Eagar, “Bringing New Materials to Market.,” *Technology Review*. vol. 98, no. 2, pp. 42–49, 1995.

[6] G. Hautier, A. Jain, and S.P. Ong, “From the computer to the laboratory: Materials discovery and design using first-principles calculations.,” *Journal of Materials Science*. vol. 47, no. 21, pp. 7317–7340, 2012.

[7] R. Ramprasad, R. Batra, G. Pilania, A. Mannodi-Kanakkithodi, and C. Kim, “Machine learning in materials informatics: Recent applications and prospects.,” *npj Computational Materials*. vol. 3, no. 1, pp. 1–13, 2017.

[8] D. Xue, P. V. Balachandran, J. Hogden, J. Theiler, D. Xue, and T. Lookman, “Accelerated search for materials with targeted properties by adaptive design.,” *Nature Communications*. vol. 7, no. 11241, pp. 1–9, 2016.

[9] G. Pilania, C. Wang, X. Jiang, S. Rajasekaran, and R. Ramprasad, “Accelerating materials property predictions using machine learning.,” *Scientific Reports*. vol. 3, no. 2810, pp. 1–6, 2013.

[10] H. Koinuma and I. Takeuchi, “Combinatorial solid-state chemistry of inorganic materials.,” *Nature Materials*. vol. 3, no. 7, pp. 429–438, 2004.

[11] M. Patel G.C, A.K. Shettigar, P. Krishna, and M.B. Parappagoudar, “Back propagation genetic and recurrent neural network applications in modelling and analysis of squeeze casting process.,” *Applied Soft Computing Journal*. vol. 59, no. 1, pp. 418–437, 2017.

[12] D.J. Leo, *Engineering analysis of smart material systems*. *John Wiley & Sons*, Hoboken, N.J., 2007.

[13] K. Uchino, *Advanced Piezoelectric Materials*. *Woodhead Publishing Ltd*, Kent, 2017.

[14] B. Jaffe, W.R. Cook, and H. Jaffe, *Piezoelectric ceramics*. *Acad. Press*, London, 1971.

[15] S. Roberts, “Dielectric and piezoelectric properties of barium titanate.,” *Physical Review*. vol. 71, no. 12, pp. 890–895, 1947.

[16] W.P. Mason, “Aging of the properties of barium titanate and related ferroelectric ceramics.,” *The Journal of the Acoustical Society of America*. vol. 27, no. 1, pp. 73–85, 1955.

[17] M. Schwartz, *The Encyclopedia of Smart Materials*. *Wiley*, New York, 2002.

[18] M. Takahashi, “Space charge effect in lead zirconate titanate ceramics caused by the addition of impurities.,” *Japanese Journal of Applied Physics*. vol. 9, no. 10, pp. 1236–1246, 1970.

[19] H. Kawai, “The piezoelectricity of poly (vinylidene fluoride).,” *Japanese Journal of Applied Physics*. vol. 8, no. 7, pp. 975–976, 1969.

[20] A. Salimi and A.A. Yousefi, “FTIR studies of b-phase crystal formation in stretched PVDF films.,” *Polymer Testing*. vol. 22, no. 6, pp. 699–704, 2003.

[21] P. Martins, A.C. Lopes, and S. Lanceros-Mendez, “Electroactive phases of poly (vinylidene fluoride): determination, processing and applications.,” *Progress in polymer science*. vol. 39, no. 4, pp. 683–706, 2014.

[22] S.M. Lebedev, O.S. Gefle, and S.N. Tkachenko, “Influence of the processing method on the properties of a PVDF film.,” *Russian Physics Journal*. vol. 54, no. 6, pp. 679–685, 2011.

[23] B.-E. El Mohajir and N. Heymans, “Changes in structural and mechanical behaviour of PVDF with processing and thermomechanical treatments. 1. Change in structure.,” *Polymer*. vol. 42, no. 13, pp. 5661–5667, 2001.

[24] J. Czochralski, “A new method for measuring the crystallization rate of metals.,” *Journal of Physical Chemistry*. pp. 219–221, 1918.

[25] T.R. Shrout, Z.P. Chang, N. Kim, and S. Markgraf, “Dielectric behavior of single crystals near the (1− X) Pb (Mg1/3Nb2/3) O3-(x) PbTiO3 morphotropic phase boundary.,” *Ferroelectrics Letters Section*. vol. 12, no. 3, pp. 63–69, 1990.

[26] J. Kuwata, K. Uchino, and S. Nomura, “Dielectric and piezoelectric properties of 0.91 Pb (Zn1/3Nb2/3) O3-0.09 PbTiO3 single crystals.,” *Japanese Journal of Applied Physics*. vol. 21, no. 9R, pp. 1298–1302, 1982.

[27] P.K. Panda and B. Sahoo, “PZT to lead free piezo ceramics: a review.,” *Ferroelectrics*. vol. 474, no. 1, pp. 128–143, 2015.

[28] E.C. Directive, “89/677/EEC of 21 December 1989 amending for the eighth time Directive 76/769 EEC on the approximation of the laws, regulations and administrative provisions of the member states relating to restrictions on the marketing and use of certain

dangerous substa.," *Official Journal of the European Union*. no. L398, pp. 19–23, 1989.

[29] E.C. Directive, "2011/65/EU of the European Parliament and of the Council of 8 June 2011, on the restriction of the use of certain hazardous substances in electrical and electronic equipment (recast).," *Official Journal of the European Union*. no. L174, pp. 88–110, 2011.

[30] E.C. Directive, "2012/19/EU of the European Parliament and of the Council of 4 July 2012 on waste electrical and electronic equipment, WEEE.," *Official Journal of the European Union*. no. L197, pp. 38–71, 2012.

[31] T. Takenaka, K. Maruyama, and K. Sakata, "(Bi1/2Na1/2) TiO3-BaTiO3 system for lead-free piezoelectric ceramics.," *Japanese journal of applied physics*. vol. 30, no. 9S, pp. 2236–2239, 1991.

[32] Y. Saito, H. Takao, T. Tani, et al., "Lead-free piezoceramics.," *Nature*. vol. 432, no. 7013, pp. 84–87, 2004.

[33] K. Xu, J. Li, X. Lv, et al., "Superior Piezoelectric Properties in Potassium–Sodium Niobate Lead- Free Ceramics.," *Advanced Materials*. vol. 28, no. 38, pp. 8519–8523, 2016.

[34] X. Liu and X. Tan, "Giant Strains in Non- Textured (Bi1/2Na1/2) TiO3- Based Lead-Free Ceramics.," *Advanced Materials*. vol. 28, no. 3, pp. 574–578, 2016.

[35] T. Ogawa and Y. Numamoto, "Origin of giant piezoelectricity in PbZnNbTiO single crystals.," *Integrated Ferroelectrics: An International Journal*. vol. 63, no. 1, pp. 21–26, 2004.

[36] T. Karaki, M. Adachi, Y. Hosono, and Y. Yamashita, "Distribution of piezoelectric properties in Pb[(Mg1/3Nb2/3)0.7Ti0.3]O3 single crystal.," *Japanese Journal of Applied Physics, Part 2: Letters*. vol. 41, no. 4 A, pp. L402–L404, 2002.

[37] R.E. Newnham, V. Sundar, R. Yimnirun, J. Su, and Q.M. Zhang, "Electrostriction: nonlinear electromechanical coupling in solid dielectrics.," *The Journal of Physical Chemistry B*. vol. 101, no. 48, pp. 10141–10150, 1997.

[38] G.A. Smolenskii, V.A. Isupov, A.I. Agranovskaya, and S.N. Popov, "Ferroelectrics with diffuse phase transitions.," *Soviet Physics-Solid State*. vol. 2, no. 11, pp. 2584–2594, 1961.

[39] K. Uchino, S. Nomura, L.E. Cross, S.J. Jang, and R.E. Newnham, "Electrostrictive effect in lead magnesium niobate single crystals.," *Journal of Applied Physics*. vol. 51, no. 2, pp. 1142–1145, 1980.

[40] S.J. Jang, K. Uchino, S. Nomura, and L.E. Cross, "Electrostrictive behavior of lead magnesium niobate based ceramic dielectrics.," *Ferroelectrics*. vol. 27, no. 1, pp. 31–34, 1980.

[41] J. Kuwata, K. Uchino, and S. Nomura, “Electrostrictive coefficients of Pb (Mg1/3Nb2/3) O3 ceramics.,” *Japanese Journal of Applied Physics*. vol. 19, no. 11, pp. 2099–2103, 1980.

[42] L.E. Cross, S.J. Jang, R.E. Newnham, S. Nomura, and K. Uchino, “Large electrostrictive effects in relaxor ferroelectrics.,” *Ferroelectrics*. vol. 23, no. 1, pp. 187–191, 1980.

[43] S. Nomura, S.J. Jang, L.E. Cross, and R.E. Newnham, “Structure and Dielectric Properties of Materials in the Solid Solution System Pb (Mg1/3Nb2/33) O3: Pb (W1/2Mg1/2) O3.,” *Journal of the American Ceramic Society*. vol. 62, no. 9- 10, pp. 485–488, 1979.

[44] G.H. Haertling, “Ferroelectric ceramics: history and technology.,” *Journal of the American Ceramic Society*. vol. 82, no. 4, pp. 797–818, 1999.

[45] A.A. Bokov and Z.-G. Ye, “Recent progress in relaxor ferroelectrics with perovskite structure.,” *Journal of Materials Science*. vol. 41, no. 1, pp. 31–52, 2006.

[46] G.A. Samara and E.L. Venturini, “Ferroelectric/relaxor crossover in compositionally disordered perovskites.,” *Phase Transitions*. vol. 79, no. 1–2, pp. 21–40, 2006.

[47] R. Fisch, “Random-field models for relaxor ferroelectric behavior.,” *Phys.Rev.B*. vol. 67, no. 9, pp. 94110–94111, 2003.

[48] C. Lei, A.A. Bokov, and Z.-G. Ye, “Relaxor Behavior in Ba(Ti0.72Sn0.28)O3 Solid Solution.,” *Ferroelectrics*. vol. 339, no. 1, pp. 129–136, 2006.

[49] D. Fu, H. Taniguchi, M. Itoh, and S. Mori, “Pb(Mg1/3Nb2/3)O3 (PMN) Relaxor: Dipole Glass or Nano-Domain Ferroelectric?,” In: *Advances in Ferroelectrics*. pp. 51–67. *Intech* (2012).

[50] M. Otonicar, A. Reichmann, and K. Reichmann, “Electric field-induced changes of domain structure and properties in La-doped PZT-From ferroelectrics towards relaxors.,” *Journal of the European Ceramic Society*. vol. 36, no. 10, pp. 2495–2504, 2016.

[51] S.L. Swartz and T.R. Shrout, “Fabrication of perovskite lead magnesium niobate.,” *Materials Research Bulletin*. vol. 17, no. 10, pp. 1245–1250, 1982.

[52] J.-H. Choy, Y.-S. Han, S.-W. Song, and S.-H. Chang, “Preparation of single-phase Pb(Mg1/3Nb2/3)O3 samples utilizing information from solubility relationships in the Pb?Mg?Nb?citric acid?H2O system.,” *Journal of Materials Chemistry*. vol. 4, no. 8, pp. 1271–1274, 1994.

[53] L.F. Francis, Y.-J. Oh, and D.A. Payne, “Sol-gel processing and properties of lead magnesium niobate powders and thin layers.,” *Journal of Materials Science*. vol. 25, no. 12, pp. 5007–5013, 1990.

[54] J.C. Carvalho, C.O. Paiva-Santos, M.A. Zaghete, C.F. Oliveira, J.A. Varela, and E. Longo, “Phase analysis of seeded and doped PbMg 1/3 Nb 2/3 O 3 prepared by organic

solution of citrates.," *Journal of Materials Research*. vol. 11, no. 7, pp. 1795–1799, 1996.

[55] K. Yanagisawa, "Formation of perovskite-type Pb (Mg 1/3 Nb 2/3) O 3 under hydrothermal conditions.," *Journal of Materials Science Letters*. vol. 12, no. 23, pp. 1842–1843, 1993.

[56] S.M. Gupta and A.R. Kulkarni, "Dielectric and microstructure studies of lead magnesium niobate prepared by partial oxalate route.," *Journal of the European Ceramic Society*. vol. 16, no. 4, pp. 473–480, 1996.

[57] S.M. Gupta and A.R. Kulkarni, "Role of excess PbO on the microstructure and dielectric properties of lead magnesium niobate.," *Journal of Materials Research*. vol. 10, no. 4, pp. 953–961, 1995.

[58] Y.K. Hyun, C. Yong- Soo, L. Dong- Heon, and K. Dong- Heon, "Powder Characteristics of Pb(Mg1/3Nb2/3)O3 Prepared by Molten Salt Synthesis.," *Journal of the American Ceramic Society*. vol. 76, no. 5, pp. 1373–1376, 2005.

[59] J. Wang, X. Junmin, W. Dongmei, and N. Weibeng, "Mechanochemical fabrication of single phase PMN of perovskite structure.," *Solid State Ionics*. vol. 124, no. 3, pp. 271–279, 1999.

[60] J. Kuwata, K. Uchino, and S. Nomura, "Phase transitions in the Pb (Zn 1/3 Nb 2/3)O 3 - PbTiO 3 system.," *Ferroelectrics*. vol. 37, no. 1, pp. 579–582, 1981.

[61] G.H. Haertling, "PLZT electrooptic materials and applications—a review.," *Ferroelectrics*. vol. 75, no. 1, pp. 25–55, 1987.

[62] A. Halliyal and A. Safari, "Synthesis and properties of lead zinc niobate: Pb(Zn1/3Nb2/3)O3 based relaxor ferroelectrics.," *Ferroelectrics*. vol. 158, no. 1, pp. 295–300, 1994.

[63] K. Otsuka and C.M. Wayman, *Shape Memory Materials*. *Cambridge University Press*, 1998.

[64] I.M. Ihálcz, "Fundamental Characteristics and Design Method for Nickel-Titanium Shape Memory Alloy.," vol. 45, no. 1, pp. 75–86, 2001.

[65] R. DesRoches, J. McCormick, and M. Delemont, "Cyclic Properties of Superelastic Shape Memory Alloy Wires and Bars.," *Journal of Structural Engineering*. vol. 130, no. 1, pp. 38–46, 2004.

[66] S. Hurlebaus and L. Gaul, "Smart structure dynamics.," *Mechanical Systems and Signal Processing*. vol. 20, no. 2, pp. 255–281, 2006.

[67] K. Otsuka and X. Ren, "Recent developments in the research of shape memory alloys.," *Intermetallics*. vol. 7, no. 5, pp. 511–528, 1999.

[68] G.A. Samara, “The relaxational properties of compositionally disordered ABO3 perovskites.,” *Journal of Physics: Condensed Matter*. vol. 15, no. 9, pp. 367–411, 2003.

[69] A. Ölander, “An electrochemical investigation of solid cadmium-gold alloys.,” *Journal of the American Chemical Society*. vol. 54, no. 10, pp. 3819–3833, 1932.

[70] A. Greninger and V. Mooradian, “Strain Transformation in Metastable Beta Copper-Zinc and Beta Copper-Ti Alloys.,” *AIME Trans*. vol. 128, no. 867, pp. 337–368, 1938.

[71] G. V Kurdjumov and L.G. Khandros, “First reports of the thermoelastic behaviour of the martensitic phase of Au-Cd alloys.,” *Doklady Akademii Nauk, SSSR*. vol. 66, pp. 211–213, 1949.

[72] L.C. Chang and T.A. Read, “Plastic Deformation and Diffusionless Phase Changes in Metals - The Gold-Cadmium Beta-Phase.,” *Transactions of the American Institute of Mining and Metallurgical Engineers*. vol. 191, no. 1, pp. 47–52, 1951.

[73] J. Mohd Jani, M. Leary, A. Subic, and M.A. Gibson, “A review of shape memory alloy research, applications and opportunities.,” *Materials and Design*. vol. 56, pp. 1078–1113, 2014.

[74] W.J. Buehler, J. V. Gilfrich, and R.C. Wiley, “Effect of Low-Temperature Phase Changes on the Mechanical Properties of Alloys near Composition TiNi.,” *Journal of Applied Physics*. vol. 34, no. 5, pp. 1475–1477, 1963.

[75] W.J. Buehler, “The unique nonmagnetic Nitinol alloys.,” *NASA Technical Report*. no. 19660002010, pp. 1–25, 1965.

[76] G.B. Kauffman and I. Mayo, “The Story of Nitinol: The Serendipitous Discovery of the Memory Metal and Its Applications.,” *The Chemical Educator*. vol. 2, no. 2, pp. 1–21, 1997.

[77] K. Otsuka and X. Ren, “Physical metallurgy of Ti–Ni-based shape memory alloys.,” *Progress in Materials Science*. vol. 50, no. 5, pp. 511–678, 2005.

[78] J. Ren and K.M. Liew, “Meshfree modelling and characterisation of thermomechanical behaviour of NiTi alloys.,” *Engineering Analysis with Boundary Elements*. vol. 29, no. 1, pp. 29–40, 2005.

[79] C. Haberland, M. Elahinia, J.M. Walker, H. Meier, and J. Frenzel, “On the development of high quality NiTi shape memory and pseudoelastic parts by additive manufacturing.,” *Smart Materials and Structures*. vol. 23, no. 104002, pp. 1–13, 2014.

[80] S. Shiva, I.A. Palani, S.K. Mishra, C.P. Paul, and L.M. Kukreja, “Investigations on the influence of composition in the development of Ni-Ti shape memory alloy using laser based additive manufacturing.,” *Optics and Laser Technology*. vol. 69, no. 1, pp. 44–51, 2015.

[81] S. Saedi, A.S. Turabi, M. Taheri Andani, C. Haberland, H. Karaca, and M. Elahinia, "The influence of heat treatment on the thermomechanical response of Ni-rich NiTi alloys manufactured by selective laser melting.," *Journal of Alloys and Compounds*. vol. 677, pp. 204–210, 2016.

[82] D.C. Lagoudas, Ed., *Shape Memory Alloys*. *Springer Science+Business Media, LLC*, New York, 2008.

[83] J. Ma, I. Karaman, and R.D. Noebe, "High temperature shape memory alloys.," *International Materials Reviews*. vol. 55, no. 5, pp. 257–315, 2010.

[84] C. Liu, H. Qin, and P.T. Mather, "Review of progress in shape-memory polymers.," *Journal of Materials Chemistry*. vol. 17, no. 16, pp. 1543–1558, 2007.

[85] J. Hu, Y. Zhu, H. Huang, and J. Lu, "Recent advances in shape-memory polymers: Structure, mechanism, functionality, modeling and applications.," *Progress in Polymer Science*. vol. 37, no. 12, pp. 1720–1763, 2012.

[86] G. Engdahl, *Handbook of Giant Magnetostrictive Materials*. *Academic Press*, 2000.

[87] A.E. Clark, "Chapter 7 Magnetostrictive rare earth-fe compounds.," In: *Handbook of Ferromagnetic Materials*. pp. 531–589 (1980).

[88] A.E. Clark and H.S. Belson, "Giant room-temperature magnetostrictions in TbFe2 and DyFe2.," *Physical Review B*. vol. 5, no. 9, pp. 3642–3644, 1972.

[89] A. E. Clark and M. Wun-Fogle, "Modern Magnetostrictive Materials – Classical and Non-Classical Alloys.," In: *Proc. SPIE 4699, Smart Structures and Materials 2002: Active Materials: Behavior and Mechanics*. pp. 421–436. *International Society for Optics and Photonics* (2002).

[90] J.H. Liu, C.B. Jiang, and H. Bin Xu, "Giant magnetostrictive materials.," *Science China Technological Sciences*. vol. 55, no. 5, pp. 1319–1326, 2012.

[91] S. Yang, H. Bao, C. Zhou, et al., "Large magnetostriction from morphotropic phase boundary in ferromagnets.," *Physical Review Letters*. vol. 104, no. 19, pp. 1–4, 2010.

[92] A. Clark, J. Teter, and O. McMasters, "Magnetostrictive properties of Tb.3Dy.7(Fe1-xCox)1.9 and Tb.3Dy.7(Fe1-xNix)1.9.," *IEEE Transactions on Magnetics*. vol. 23, no. 5, pp. 3526–3528, 1987.

[93] L. Xu, C. Jiang, and H. Xu, "Magnetostriction and electrical resistivity of Si doped Tb0.3 Dy0.7 Fe1.95 oriented crystals.," *Applied Physics Letters*. vol. 89, no. 19, p. 192507, 2006.

[94] A.E. Clark, J.B. Restorff, M. Wun-Fogle, T.A. Lograsso, and D.L. Schlagel, "Magnetostrictive properties of body-centered cubic Fe-Ga and Fe-Ga-Al alloys.," *IEEE Transactions on Magnetics*. vol. 36, no. 5 I, pp. 3238–3240, 2000.

[95] F.G. Yuan, “Magnetostrictive Materials.,” In: *Structural Health Monitoring*. pp. 41. *North Carolina State University, Raleigh* (2018).

[96] A.J. Moulson and J.M. Herbert, *Electroceramics*. *Wiley*, Hoboken, 2003.

[97] “APC International, Ltd.,” https://www.americanpiezo.com/.

[98] I. Ben-Gal, “Outlier Detection.,” In: *Data Mining and Knowledge Discovery Handbook*. pp. 131–146. *Springer-Verlag*, New York (2005).

[99] M. Dash, H. Liu, and J. Yao, “Dimensionality Reduction for Unsupervised Data.,” In: *Ninth IEEE International Conference on Tools with Artificial Intelligence (ICTAI ’97)*. pp. 532–539. *IEEE Comput. Soc* (1997).

[100] D.E. Rumelhart, G.E. Hinton, and R.J. Williams, “Learning representations by back-propagating errors.,” *Nature*. vol. 323, no. 6088, pp. 533–536, 1986.

[101] I. Goodfellow, Y. Bengio, and A. Courville, *Deep learning*. *MIT Press*, 2016.

[102] M. Nielsen, *Neural Networks and Deep Learning*. *Determination Press*, 2015.

[103] X. He, W.-J. Ding, and X.-S. Yang, “Bat algorithm based on simulated annealing and Gaussian perturbations.,” *Neural Computing and Applications*. vol. 25, no. 2, pp. 459–468, 2014.

[104] A.J. Keane, “Genetic algorithm optimization of multi-peak problems: studies in convergence and robustness.,” *Artificial Intelligence in Engineering*. vol. 9, no. 2, pp. 75–83, 1995.

[105] V.K. Singla, “Github,” https://github.com/vsingla2/Cascaded-Neural-Net.